Disparate evolution mechanisms and optical absorption for transboundary soot particles passing through inland and sea pathways

Jian Zhang[1], Zexuan Zhang[2], Keliang Li[2], Xiyao Chen[2], Xinpeng Xu[2], Yangmei Zhang[3], Anzhou Han[4], Yuanyuan Wang[5], Jing Ding[1], Liang Xu[6], Yinxiao Zhang[7], Hongya Niu[8], Shoujuan Shu[2], and Weijun Li[2,*]

[1]School of Environmental and Material Engineering, Yantai University, Yantai 264005, China

[2]Key Laboratory of Geoscience Big Data and Deep Resource of Zhejiang Province, Department of Atmospheric Sciences, School of Earth Sciences, Zhejiang University, Hangzhou 310027, China

[3]Key Laboratory of Atmospheric Chemistry, China Meteorological Administration, Beijing 100081, China

[4]Trier College of Sustainable Technology, Yantai University, Yantai 264005, China

[5]Hangzhou International Innovation Institute of Beihang University, Hangzhou 310000, China

[6]College of Sciences, China Jiliang University, Hangzhou 310018, China

[7]Flight College, Shandong University of Aeronautics, Binzhou 256600, China

[8]Key Laboratory of Resource Exploration Research of Hebei Province, Hebei University of Engineering, Handan 056038, China

[*]Corresponding Email: liweijun@zju.edu.cn (W. J. Li)

Abstract

Soot particles, as a type of warming aerosols, play a critical role in climate warming. During transport, these particles undergo atmospheric condition-dependent aging processes that influence their microphysical and optical properties. Here, we investigated the variations in morphology, mixing structures, sizes, and optical absorption of soot-containing particles and further revealed their evolution mechanisms during two distinct transboundary transport through the inland and sea pathways. Comparing transboundary soot-containing particles transported through the inland and sea pathways, we found more soot cores in the latter individual particles, although their dominant mixing structures exhibited a similar transition from partly-coated at 62-67% by number to embedded structures at 71-72%. The core-shell size ratio (D_p/D_c) and soot core fractal dimension of embedded soot-containing particles transported through the sea pathway were both greater compared to the inland pathway. These differences were attributed to distinct evolution mechanisms experienced by soot-containing particles during transport: heterogeneous aging processes through the inland pathway and cloud processes through the sea pathway. Optical simulation showed amplified light absorption of soot-containing particles during their transboundary transport. Furthermore, the radiative absorption amplification per unit D_p/D_c change reduced by 72% due to the entrainment of multiple soot cores within individual particles following the transport pathway change from the inland to the sea. This study suggests varied mixing configurations and radiative absorption of transboundary soot-containing particles driven by different environmental conditions and highlights the necessity of incorporating multicore black carbon mixing structures into climate models.

1. Introduction

In recent years, eastern China still faces severe haze pollution in winter despite a series of control policies adopted by the local government (Peng et al., 2021; Zang et al., 2022; Zhai et al., 2021). High concentrations of fine haze particles not only affect human health (Geng et al., 2021; Zhang et al., 2017b), but also influence the global climate (Li et al., 2016a; Suzuki and Takemura, 2019). In addition to high emissions of pollutants and stable meteorological conditions (Niu et al., 2016; Zhao et al., 2019; Zheng et al., 2015), transboundary transport of pollutants has been confirmed to be an important factor causing the formation of regional haze pollution in eastern China in winter (Li et al., 2019; Zhang et al., 2021; Zhang et al., 2019a). For example, large amounts of haze pollutants in the North China Plain (NCP) can be transported thousands of kilometers to the Yangtze River Delta (YRD) under cold fronts to induce long-lasting regional haze events (Huang et al., 2020).

In eastern China, the NCP and the YRD as two rapid economic developed regions suffer the heaviest haze pollution (Zhong et al., 2019). Recent studies found frequent transboundary transport of pollutants from the NCP to the YRD using various methods including field observation and model simulation (Kang et al., 2019; Li et al., 2019; Xie et al., 2023; Yan et al., 2024; Zhang et al., 2021). For instance, Kang et al. (2019) utilized numerical models to show that the $PM_{2.5}$ contribution from the NCP reached to ~30% in the YRD under cold fronts. Field results showed that concentrations of organic matter and secondary inorganic ions in $PM_{2.5}$ in the YRD increased by approximately 1-2 times following the invasion of haze pollutants from the NCP (Zhang et al., 2021). Xie et al. (2023) also suggested that carbonaceous aerosols and secondary inorganic ions were effectively transported from the NCP to the YRD based on the simulation of the average atmospheric age of haze particles. During the transboundary transport, abundant secondary aerosols (e.g., sulfate and nitrate) can be formed through heterogeneous chemical processes, influencing the particulate hygroscopicity (Li et al., 2019; Li et al., 2025; Zhang et al., 2021). Although these studies revealed changes in the bulk chemical composition of fine particles and main formation processes of

secondary aerosols during the transport, there is a lack of evolution mechanisms of transboundary particles and their potential health or climate effects.

We noticed that cold fronts had different pathways to convey air pollutants from the NCP to the YRD depending on the location of high-pressure systems. The previous studies showed that cold fronts from the high-pressure system locating in the west of the NCP normally transported haze pollutants across city clusters in eastern China (Hou et al., 2020; Jin et al., 2021). If the high-pressure system is located in the interior of the NCP, heavy haze covering the Jing-Jin-Ji region (i.e., Beijing, Tianjin, and Hebei) could move out from inland China to the East China Sea and return into the inland region under prevailing winds, influencing air quality of the YRD (see section 3.1). These haze movements from the NCP to the YRD were clearly observed from the satellites (https://worldview.earthdata.nasa.gov). To our knowledge, the previous studies only focused on the haze transportation from the NCP to the YRD through the inland pathway based on field measurements and model simulation (Huang et al., 2020; Yan et al., 2024). Obviously, there is a bench of data available from national ground monitoring net station of air quality to support the measurements and modelling studies. However, transboundary haze pollutants crossing the East China Sea remain unexplored. We expect different chemical mechanisms and aging processes in gas-aerosol interactions in two haze layers because of different meteorological factors (e.g., relative humidity) and pollutant emissions in transport pathways.

Soot particles dominated by black carbon, mainly emitted from incomplete burning of fossil, biomass, and other non-biological fuels, are important light absorbing aerosols in fine particles (Bond et al., 2013). They exert positive radiative forcing effects on global warming in the atmosphere (Cappa et al., 2012; Jacobson, 2001). Soot particles serve as an excellent tracer to reflect atmospheric aging because their morphology (Fierce et al., 2020; Wu et al., 2018; Yuan et al., 2019), mixing states (Wang et al., 2019; Wang et al., 2016), sizes (Adachi et al., 2014; Xu et al., 2020), and mass (Liu et al., 2020; Zhang et al., 2018) can be significantly altered during transport. Previous global studies examining pollutant transport, such as trans-oceanic dust events

affecting East Asia (Xu et al., 2020) and North America outflow influencing the Azores in the North Atlantic (China et al., 2015), have extensively utilized soot particles as a primary investigative target to understand environmental impacts. The transport corridor from the NCP to the YRD represents no exception, where soot particles persist as a critical, abundant component of atmospheric aerosols (Huang et al., 2020; Zhang et al., 2023). Compared to transport over inland China, soot particles transported to the YRD from the NCP via the East China Sea may encounter more humid conditions. These distinct atmospheric environments can lead to different alterations in soot physicochemical properties (Li et al., 2024). Therefore, the evolution of soot particles and their environmental and climate impacts should be examined in different synoptic weather processes. When simulating soot climate effect in models, the complicated microphysical properties of soot particles could be underestimated due to limited studies, thereby introducing considerable uncertainties into the results (Chen et al., 2025; IPCC, 2021).

To bridge this critical gap, we observed two types of transboundary transport events of haze pollutants (passing through the inland and through the sea pathways) from the NCP to the YRD and first compared physicochemical characteristics (e.g., morphology, mixing structures, and sizes) of transboundary soot particles in the two events by various microscopic measurements. Based on microscopic observations, the evolution mechanisms of two types of transboundary soot particles were unveiled. Using a novel optical calculation model, we further estimated the change in soot optical absorption between two types of transboundary transport. This study aims to emphasize how divergent transport environments (inland vs. sea) impart distinct physicochemical effects on soot particles. This promotes understanding of the weather-aerosol-pollution-climate nexus, ultimately informing more accurate prediction of soot role in regional climate forcing and atmospheric chemistry.

2. Methods

2.1 Sample collection

Three sites (Beijing, Handan, and Zhengzhou) in the NCP and two sites (Nanjing and Hangzhou) in the YRD were selected to collect ambient $PM_{2.5}$ and individual aerosol particles in December 2017 and 2020 based on the transport behavior of airborne pollutants under cold fronts in winter (Figure S1). Beijing, Handan, and Zhengzhou are located in the northern, central, and southern parts of the NCP, respectively. Beijing is a typical megacity and influenced by local emissions and regional transport, while Handan and Zhengzhou are two typical industrial cities and affected by local industrial, vehicular, and residential emissions. Nanjing and Hangzhou are two megacities located in the northern and southern parts of the YRD. These two megacities can be influenced when haze particles in the NCP invade the YRD. Therefore, the above five cities in the NCP and YRD are representative for exploring transboundary transport of aerosols (e.g., soot particles) in haze plumes. The detailed information of the sampling sites has been described in previous studies (Zhang et al., 2023; Zhang et al., 2021).

Ambient $PM_{2.5}$ and blank samples (no pumping) were collected on preheated quartz filters with 90 mm diameters (600°C for 4 hr, Whatman) twice a day from 8:30 (local time) to 20:00 and from 20:30 to 8:00 the next day using medium volume samplers (TH-16A, Wuhan Tianhong, 100 L min^{-1}). Individual aerosol particles were sampled on transmission electron microscopy (TEM) grids and silicon wafers four times a day at around 2:00 (local time), 9:00, 14:00, and 20:00 utilizing individual particle samplers (DKL-2, Genstar, 1 L min^{-1}) equipped with a 0.5 mm jet nozzle impactor. To avoid particles overlapping on the substrate, the sampling duration of individual particles needs to be adjusted from 30 s to 15 min according to current $PM_{2.5}$ concentrations from 17 μg m^{-3} to 320 μg m^{-3}. Hourly $PM_{2.5}$ concentrations and meteorological parameters including relative humidity (RH) and winds were derived from local monitoring stations (https://www.aqistudy.cn/).

2.2 $PM_{2.5}$ and individual particle analyses

Water-soluble inorganic ions (i.e., NO_3^-, SO_4^{2-}, NH_4^+, F^-, Cl^-, Na^+, K^+, Ca^{2+}, and

Mg^{2+}), carbonaceous components (organic and elemental carbon), and trace metallic elements in $PM_{2.5}$ samples were analyzed using an ion chromatography system (Dionex ICs-90, USA), an OC/EC analyzer (Sunset Laboratory, USA), and inductively coupled plasma mass spectrometry (ICP-MS, Agilent 7500ce). The detailed experimental processes can be found in previous studies (Pan et al., 2013; Zhang et al., 2017a). Considering the contribution of other elements (e.g., O, H, N, and S) to the mass of organic matter (OM, i.e., organic compound), OM concentrations were obtained by multiplying organic carbon (OC) concentrations by 1.91 reported by Xing et al. (2013).

Morphology, mixing states, and compositions of individual aerosol particles collected on TEM grids were examined by TEM equipped with energy-dispersive X-ray spectrometry (EDS) (JEM-2100, JEOL). The acquisition time of TEM images and EDS spectra is usually controlled within 15 s because of the damage of electron beams to non-refractory aerosols. To better observe soot mixing structures and measure soot geometrical parameters, we enhanced the electron beam to sublime non-refractory coatings of indiscernible soot cores after conventional TEM observations. Copper element was excluded from particle EDS spectra because TEM grids are made of copper (Li et al., 2025). Using an image analysis software (Radius, EMSIS GmbH), we further obtained the equivalent circle diameter (ECD), length, and area of particles in TEM images. These parameters for indiscernible soot particles were measured under TEM observations with the enhanced electron beam. In this work, 3642 individual particles were analyzed by TEM in total.

Three-dimensional morphology of individual particles collected on silicon wafers was probed by atomic force microscopy (AFM, Dimension Icon) in tapping mode. Employing a professional image analysis software (NanoScope Analysis), the bearing area (A) and the bearing volume (V) of particles in AFM images were quantified. The ECD and the equivalent sphere diameter (ESD) of these particles can be calculated applying equations (1) and (2).

$$ECD = \sqrt{\frac{4A}{\pi}} \quad (1)$$

$$ESD = \sqrt[3]{\frac{6V}{\pi}} \quad (2)$$

Figure S2 shows that there is a good correlation between the ESD and the ECD with slopes at 0.62 for passing through the inland pathway transport and 0.39 for passing through the sea pathway transport. According to the relationship between the ESD and the ECD, ESDs of particles observed by TEM were computed. The ESDs of soot particles were perceived as equivalent to their ECDs because they are composed of solid carbonaceous spheres that are not affected by substrates in terms of morphology (Barone et al., 2012; Li et al., 2016b).

The size ratio of soot-containing particles to their soot cores (D_p/D_c) was evaluated using equation (3):

$$D_p/D_c = \frac{ESD_{soot\text{-}containing}}{ESD_{soot}} \quad (3)$$

where $ESD_{soot\text{-}containing}$ is the ESD of soot cores with their coatings and ESD_{soot} is the soot core ESD. The volume ratio of soot coatings to soot cores ($V_{coating}/V_c$) was further calculated according to the D_p/D_c.

Based on the scaling law in the following equation, we obtained the fractal dimension (D_f) of soot particles, which can be used to reflect the compactness of soot particles:

$$N = k_g \left(\frac{2R_g}{d_p}\right)^{D_f} \quad (4)$$

where N is the monomer number in soot particles, k_g is the fractal prefactor, R_g is the gyration radius of soot particles, and d_p is the average diameter of soot monomers.

The monomer number in soot particles and the gyration radius of soot particles can be calculated using the following equations:

$$N = k_a \left(\frac{A_a}{A_p}\right)^{\alpha} \quad (5)$$

$$\frac{L_{max}}{2R_g} = 1.50 \pm 0.05 \quad (6)$$

where A_a is the projected area of soot particles, A_p is the average projected area of soot monomers, k_a is a constant, α is an empirical projected area exponent, and L_{max} is the

maximum length of soot particles.

Because the fractal prefactor is highly affected by the overlap between soot monomers (Lapuerta et al., 2015), an overlap parameter needs to be considered:

$$\delta = \frac{2a}{l} \tag{7}$$

where δ is the overlap parameter of soot monomers, a is the average radius of adjacent soot monomers, and l is the spacing of adjacent soot monomers. k_a and α depend on δ (Oh and Sorensen, 1997). Details can be found in Wang et al. (2017).

2.3 Meteorological fields and geographic sources

Wind fields coupled with surface $PM_{2.5}$ concentrations covering eastern China were obtained from European Centre for Medium-Range Weather Forecasts (ECMWF, https://earth.nullschool.net/). Meteorological fields including winds and relative humidity (RH) in eastern China at 1000 hPa were simulated using 1° × 1° Final Reanalysis Data (FNL) from the National Centers for Environmental Prediction (NCEP, https://rda.ucar.edu/datasets/ds083.2/).

The potential geographic sources of $PM_{2.5}$ at observation sites (Nanjing and Hangzhou) in the YRD were identified based on the concentration-weighted trajectory (CWT) analysis. In this study, 72 hr of air mass backward trajectories simulated from the wind data sets in the Nation Oceanic Atmospheric Administration (NOAA, ftp://arlftp.arlhq.noaa.gov/pub/archives/gdas1) were used for the CWT analysis. The resolution of CWT trajectories consists of thousands of grid cells is 0.3° × 0.3°. The equation for the CWT analysis is as follows:

$$C_{ij} = \frac{1}{\sum_{k=1}^{N} \tau_{ijk}} \sum_{k=1}^{N} C_k \tau_{ijk} \tag{8}$$

where C_{ij} is the average $PM_{2.5}$ concentration in a grid cell (i, j); C_k is the measured $PM_{2.5}$ concentration for the trajectory k arriving at the observation site; τ_{ijk} is the number of trajectory endpoints in the grid cell (i, j) for the C_k sample; N is the number of samples with trajectory endpoints in the grid cell (i, j).

In the CWT analysis, a weighing function as shown in equation (9) was applied to

further improve the CWT accuracy:

$$W=\begin{cases}1 & \text{for } \log(n+1) \geq 0.85\times\max_{\log(n+1)} \\ 0.725 & \text{for } 0.6\times\max_{\log(n+1)} \leq \log(n+1) < 0.85\times\max_{\log(n+1)} \\ 0.475 & \text{for } 0.35\times\max_{\log(n+1)} \leq \log(n+1) < 0.6\times\max_{\log(n+1)} \\ 0.175 & \text{for } \log(n+1) < 0.35\times\max_{\log(n+1)}\end{cases} \quad (9)$$

where W is weighting factor; n is the number of all trajectory endpoints in a grid cell; log(n+1) represents the density of trajectories.

2.4 Optical calculation

The Electron-Microscope-to-BC-Simulation (EMBS) tool developed by Wang et al. (2021) was used to model morphology and mixing structures of soot particles. The EMBS tool capable of building various soot-containing particle models can be applied in DDSCAT 7.3 to calculate soot optical properties based on the discrete dipole approximation (DDA). DDA is completely flexible to the geometry of object particles under the condition that the inter dipole separation d follows $|m|kd < 0.5$ and $k = 2\pi/\lambda$, where m is the refractive index of particles and λ is the incident light wavelength. To minimize DDA uncertainty, the dipole size is much smaller than the soot monomer size. Based on sizes and mixing structures of soot-containing particles as well as D_f and numbers of soot cores obtained from microscopic analyses, we employed EMBS and DDSCAT 7.3 to calculate the light absorption enhancement (E_{abs}) of soot-containing particles relative to their soot cores at 550 nm λ. In this study, soot-containing particles with one, two, and three or more soot cores were distinguished. The volumes of soot cores and their coatings remained constant in the optical calculation. The refractive indices of soot cores and coatings were considered as $1.85 + 0.71i$ (Bond and Bergstrom, 2006) and $1.53 + 0i$ (Worringen et al., 2008), respectively. Details about the EMBS and DDSCAT 7.3 can be found in the previous study (Wang et al., 2021).

3. Results and discussion

3.1 Determination of two types of transport models

Figures S3a-b show variations in hourly winds and $PM_{2.5}$ concentrations at the

observation sites in the NCP and the YRD from December 28 to 31, 2017 and from December 5 to 8, 2020. Based on the association between $PM_{2.5}$ concentrations and prevailing winds described in Text S1, we inferred that there was a typical transboundary transport process of pollutants from the NCP to the YRD on December 30-31, 2017 and December 7-8, 2020, respectively. Similar changes in $PM_{2.5}$ concentrations accompanied by winds were also found in many transboundary transport events of pollutants (Wu et al., 2022; Xie et al., 2023; Yan et al., 2024; Zhao et al., 2021).

Figure 1 displays meteorological fields coupled with surface $PM_{2.5}$ concentrations in eastern China during two transboundary transport events of pollutants. In the first transport event, the wind blew from the NCP through the inland pathway towards the YRD under the high-pressure system located in the west of the NCP (Figures 1a, 1c, and S3c). This meteorological field was similar to those of transboundary transport haze events from the NCP to the YRD across inland areas (Hou et al., 2020; Hu et al., 2021; Zhang et al., 2023). It is interesting that there was a significant change in the wind field following the high-pressure system movement to the interior of the NCP during the second transport event compared to the first event, manifested as the wind mainly blowing from the NCP to the East China Sea and then to the YRD (Figures 1b, 1d, and S3d). Such wind patterns were observed not only in the second event but also in other periods, as shown in Figure S4. Although a previous study also discovered comparable wind fields between the NCP and the YRD using a weather model, the changes in chemical compositions and microphysical properties of haze particles have not been defined during the transboundary transport (Wu et al., 2022). To determine whether the transport pathway of pollutants was consistent with the wind field, the $PM_{2.5}$ transport pathway was simulated based on the 72 hr CWT analysis (Figure 2). Figure 2 shows that $PM_{2.5}$ in Nanjing and Hangzhou was mainly transported from the NCP through the inland pathway during the first transport event but through the sea pathway during the second transport event. Therefore, we concluded two transport models of haze pollutants from the NCP to the YRD, namely passing through the inland and through

the sea pathways.

During two transboundary transport events, concentrations of chemical compositions in $PM_{2.5}$ in the NCP and the YRD significantly changed (Figure S5). The concentration of secondary inorganic ions in the NCP decreased from 92-126 μg m^{-3} during the polluted period to 28-30 μg m^{-3} during the clean period (Figure S5). OM and EC concentrations in the NCP also decreased from 43-76 μg m^{-3} and 1.5-2.1 μg m^{-3} during the polluted period to 17-31 μg m^{-3} and 0.7-0.9 μg m^{-3} during the clean period (Figure S5). Following the transportation of large amounts of pollutants from the NCP to the YRD, the concentrations of secondary inorganic ions, OM, and EC in the YRD increased from 28-37 μg m^{-3}, 13-19 μg m^{-3}, and 1.0-1.4 μg m^{-3} during the clean period to 63-65 μg m^{-3}, 32-36 μg m^{-3}, and 1.6-2.7 μg m^{-3} during the polluted period, respectively (Figure S5). These results suggest that many primary and secondary aerosols including EC were transported from the NCP to the YRD under cold fronts, both through the inland and the sea pathways. This is consistent with previous studies on the transboundary transport of haze aerosols from the NCP to the YRD (Huang et al., 2020; Li et al., 2019; Xie et al., 2023). In summary, we can confirm that these two events represent typical cases of transboundary transport of haze pollutants from the NCP to the YRD through the inland and the sea pathways.

Based on simulated meteorological fields, we noticed that polluted air masses passing through the sea pathway underwent wetter environment during transboundary transport compared to that passing through the inland pathway (Figures 1c-d). Table S1 also shows much higher average RH at 90% in the YRD following the transport of haze pollutants from the NCP to the YRD through the sea pathway in contrast to the inland pathway (RH = 83%). High RH can contribute to the transformation of microphysical properties (e.g., mixing structures, sizes, and morphology) of soot particles in the atmosphere, but the reaction mechanism may vary under different high RH levels (Fu et al., 2022; Zhang et al., 2023). Consequently, we further investigated and compared the microscopic characteristics of soot particles during their transboundary transport through the inland and through the sea pathways.

3.2 Classification and fraction change of soot particles: inland vs. sea

Based on morphology, components, and mixing states of individual transported particles examined by TEM-EDS, they were classified into soot-containing, S-OM/metal/fly ash/mineral, S-rich, and OM/metal/fly ash/mineral particles (Figure S6). The specific classification criteria were described in Text S2. Figure S6 shows that the number fraction of soot-containing particles in the NCP decreased from 45% and 51% during the polluted period to 13% and 18% during the clean period following transboundary transport of haze plumes through the inland and the sea pathways. When large amounts of haze pollutants were transported into the YRD from the NCP through the inland and the sea pathways, the number fraction of soot-containing particles in the YRD increased from 38% and 34% during the clean period to 53% and 65% during the polluted period (Figure S6). The change in the number fraction of soot-containing particles in the NCP and the YRD during transboundary transport is consistent with the variation of EC concentrations. These results suggest that abundant soot-containing particles in the NCP were transported to the YRD following transboundary transport of haze plumes.

The morphology and mixing structures of soot particles can be changed during transport due to atmospheric aging (Li et al., 2024). Figure 3 shows morphology of soot particles and their mixing structures with other aerosol components observed by TEM. Based on the mixing structure of soot particles, they were divided into three categories: bare-like, partly-coated, and embedded soot particles (Figure 3). Bare-like soot particles are characterized by being isolated and externally mixed with other aerosols (Figure 3a). Partly-coated soot particles manifest as a portion of them being coated by other aerosol components (Figure 3b). Embedded soot particles mean they are completely enveloped by other aerosol materials (Figure 3c). Among these three types of soot particles, bare-like soot particles were considered to be more freshly emitted, while embedded soot particles were more aged (China et al., 2015). To observe some indiscernible embedded soot particles more clearly, their non-refractory coatings (e.g.,

S-rich particles) were sublimed under an enhanced electron beam (Figure 3c). In some individual soot-containing particles, thin halos around aerosol components were observed (Figure 3c). These thin halos have been confirmed to be water rims left by the dehydrating of aqueous particles because their EDS spectra are similar to the substrate but different from the organic coating (Zhang et al., 2023). Therefore, soot aggregates with water rims were identified as a type of embedded soot particles.

TEM observations showed that there were different numbers of soot cores in individual soot-containing particles during transboundary transport (Figure 4a). Based on the number of soot cores in individual soot-containing particles, we further divided partly-coated soot-containing particles and embedded soot-containing particles into them with 1 soot core, 2 soot cores, and ≥ 3 soot cores (Figure 4a). In this study, less than 10% of soot-containing particles had both embedded and partly-coated soot cores. To categorize these particles, we classified those with more than 95% of the total soot volume embedded in host particles as embedded soot-containing particles, and the remainder as partly-coated types. Because these particles were relatively few, they had a limited impact on the statistical results. Figures 4b-c show the variation in the number fraction of soot-containing particles with different mixing structures and soot core numbers during transboundary transport through the inland and the sea pathways. During the polluted period, partly-coated types were dominant in soot-containing particles in the NCP, accounting for 62-67% (Figures 4b-c). Following the transboundary transport of haze plumes through the inland pathway, the dominated soot-containing particles changed from partly-coated at 67 ± 4% by number in the NCP to embedded types at 71 ± 7% in the YRD (Figure 4b). Meanwhile, more than 75% of them had one soot core (Figure 4b). However, we noticed that the soot core number in the dominated soot-containing particles increased from 1 in the NCP to ≥ 3 in the YRD in addition to the change in the dominated mixing structures from partly-coated at 62 ± 1% by number to embedded ones at 72 ± 4% when plentiful soot-containing particles were transported through the sea pathway (Figure 4c). These results indicate that soot-containing particles may be subject to different aging processes during their

transboundary transport through the inland and the sea pathways. Moreover, large numbers of soot-containing particles with multiple soot aggregates were also observed in an aged atmospheric environment (Wu et al., 2016). However, their aging mechanisms were not effectively elucidated. The potential aging mechanisms for soot-containing particles in two transboundary transport events are discussed in the following section.

3.3 Variation in microphysical characteristics of soot particles and potential aging mechanisms: inland vs. sea

Figure 5 shows number percentages of bare-like, partly-coated, and embedded soot-containing particles with different numbers of soot cores in different size bins in the NCP and the YRD during two transboundary transport events. Figure 6 displays size distributions of partly-coated and embedded soot-containing particles during their transboundary transport. Bare-like soot particles were mainly concentrated in the finer size range of 0-200 nm during the transboundary transport (Figure 5). In the NCP, partly-coated soot-containing particles with 1 soot core dominated soot-containing particles and mainly distributed in the size range of 200-500 nm during the polluted period (Figures 4b, c and 5a, c). Figure 6a, c shows consistent results that the size distribution of partly-coated soot-containing particles in the NCP had a peak at 396 nm for the transportation through the inland pathway and at 384 nm for the transportation through the sea pathway. As embedded soot-containing particles became the dominant type during the transboundary transport, their size distribution presented a peak at a larger diameter of 505 nm (inland) and at a much larger diameter of 925 nm (sea) compared to the former diameters at 464 nm and 446 nm (Figure 6). The peak diameter at 505 nm for embedded soot-containing particles transported through the inland pathway is close to ~550 nm of aged soot-containing particles during regional haze reported by Wang et al. (2019). Although number fractions of these embedded soot-containing particles with 1 core were high in both the 500-600 nm and 600-700 nm bins (Figure 5b), the absolute number in the 500-600 nm range was approximately twice

higher than that in the 600-700 nm range. As a result, the preponderant soot-containing particles in the YRD, i.e., embedded ones with 1 core (inland) and ≥ 3 cores (sea), dominated in the coarser size range of 500-600 nm and in the much coarser size range of > 1600 nm, respectively (Figure 5b, d). These findings suggest that aging processes of soot-containing particles during the transboundary transport through the sea pathway not only acquired more soot cores but also greatly enlarged their sizes in contrast to the inland pathway. Consistently, high numbers of soot cores were found in coarse particles of ≥ 800 nm during transboundary transport of biomass burning emissions (Chen et al., 2023).

The D_p/D_c and $V_{coating}/V_c$ ratios of transboundary soot-containing particles were calculated to reflect the coating thickness of soot particles and to quantify the aging degree of soot particles (Figure 7 and Table S2). During two transboundary transport events, the mean D_p/D_c ratios of partly-coated and embedded soot-containing particles presented similar levels at 2.37-2.41 and 2.85-2.92 in the NCP (Figure 7). Correspondingly, the mean $V_{coating}/V_c$ ratios remained at 12-13 and 22-24 (Table S2). Following the transboundary transport of soot-containing particles through the inland pathway, the mean D_p/D_c ratios of partly-coated and embedded soot-containing particles increased from 2.37 ± 1.27 and 2.85 ± 1.89 in the NCP to 2.79 ± 1.37 and 3.41 ± 1.87 in the YRD ($P < 0.05$, Figure 7a). Their mean $V_{coating}/V_c$ ratios also increased from 12 and 22 in the NCP to 21 and 39 in the YRD (Table S2). This amount of increase for the D_p/D_c ratio of soot-containing particles is comparable to that from ~1.8 to ~2.2 during haze evolution (Zhang et al., 2019b) and from 1.42 to 1.78 during dust storm transport (Xu et al., 2020). Moreover, consistent with these studies, we observed a transition in the dominant mixing structure of soot particles with secondary coatings from partly-coated with single soot core to embedded with single soot core configurations during the transboundary transport through the inland pathway (Figure 4b), indicating that coagulation played a negligible role in the aging process (China et al., 2015). Soot particles have been demonstrated to provide a substrate for the formation of secondary aerosols via heterogeneous or aqueous-phase reactions (Farley

et al., 2023; Han et al., 2013; Zhu et al., 2025). Figure 8 displays mixing structures of soot-containing particles when they invaded into the YRD through the inland and the sea pathways. It is noted that water rims around soot-containing particles transported through the inland pathway were not observed (Figure 8a, c-d). This implies that aqueous-phase chemistry contributed minimally to secondary aerosol formation on soot particles during the transboundary transport through the inland pathway. As a result, heterogeneous aging processes might mainly drive the enhancement of secondary aerosols on soot-containing particles transported through the inland pathway and enlarged their D_p/D_c ratios.

When soot-containing particles were transported from the NCP to the YRD through the sea pathway, the partly-coated D_p/D_c ratio slightly increased from 2.41 ± 1.37 to 2.66 ± 1.58, but the embedded D_p/D_c ratio significantly increased from 2.92 ± 2.01 to 4.38 ± 2.92 ($P < 0.001$, Figure 7b). Consistently, the mean $V_{coating}/V_c$ ratios increased from 13 for the partly-coated structure and 24 for the embedded structure to 18 and 83 (Table S2). Similar results were also found in cloud processes with the D_p/D_c increase from 2.3 to 4.4 for embedded soot-containing particles reported by Fu et al. (2022). Moreover, Xu et al. (2020) showed a relatively high D_p/D_c increase proportion of soot-containing particles during the transportation of dust storms from China across the East China Sea to Japan. Based on observed and simulated RH in eastern China (Table S1 and Figures 1c-d), soot-containing particles could experience wetter environments with > 90% RH during transboundary transport through the sea pathway compared with the inland pathway. We indeed observed obvious water rims around soot-containing particles transported through the sea pathway compared to the inland pathway (Figure 8). The presence of water rims indicates that those soot-containing particles were in the aqueous phase prior to being analyzed by TEM under vacuum (Zhang et al., 2023). Laboratory studies have also observed water rims after aqueous-phase particles are dehydrated (Sun et al., 2018). In other words, if particles undergo aqueous-phase processing during transport, and then effloresce under low RH conditions, the water rim will be present as a marker. Additionally, Liu et al. (2018)

revealed pronounced aqueous-phase signatures surrounding cloud droplet residuals, as indicated by water rims. AFM measurements further confirmed that the particles transported through the sea pathway exhibited a droplet morphology (Figure S2b). It is noted that the peak diameter and core number of embedded soot-containing particles largely shifted from 446 nm and 1 to 925 nm and ≥ 3 during transboundary transport through the sea pathway (Figures 4c and 6c-d). The evolution implies that simple coagulation or condensation was not the primary aging processes of soot-containing particles in high RH environments, because these mechanisms are insufficient to explain the observed micron-sized particles with multiple cores (Liu et al., 2018). Instead, cloud processing likely played a more important role. Figure S7 shows the satellite image combined with the backward trajectory of haze masses during December 7-8, 2020. We found the presence of clouds over the East China Sea during the transport of haze masses through the sea pathway (Figure S7). Moreover, the observed phenomenon of two or more soot cores within individual particles transported through the sea pathway aligns with the findings that a single cloud droplet can entrain numerous refractory aerosol particles (e.g., soot) (Ding et al., 2025; Liu et al., 2018). We further noticed that soot-containing particles did not pass areas with high emissions during transboundary transport through the sea pathway compared to those transported through the inland pathway (Figures 1a-b). These findings suggest that the aging process of soot-containing particles was primarily driven by the meteorological change (i.e., cloud), with minimal contribution from additional industrial and urban emissions along the sea pathway. Therefore, soot-containing particles predominantly underwent cloud process aging during the transboundary transport through the sea pathway, resulting in a significant thickening of coatings on soot cores.

The D_f of soot particles serves as a critical metric for assessing their compactness and degree of atmospheric aging processes, providing a quantitative basis for black carbon characterization (Li et al., 2024; Pang et al., 2022). Figure 9 presents the evolution of D_f for partly-coated and embedded soot particles during atmospheric transport through the inland and sea pathways. The D_f of partly-coated and embedded

soot particles increased from 1.81 ± 0.03 and 1.90 ± 0.03 in the NCP to 1.84 ± 0.06 and 1.93 ± 0.04 in the YRD following the transboundary transport through the inland pathway (Figures 9a-b), suggesting that secondary coatings formed via heterogeneous aging processes enhanced soot compactness during the transport. This varied result of soot D_f during the transboundary transport through the inland pathway is similar to that during the dynamic progression of regional heavy haze pollution in winter (Zhang et al., 2023). However, when soot particles were transported to the YRD from the NCP through the sea pathway, their D_f increased from 1.81 ± 0.05 for partly-coated soot and 1.89 ± 0.06 for embedded soot to 1.85 ± 0.06 and 2.07 ± 0.03 (Figures 9c-d). This suggests that the structural collapse of embedded soot particles was more pronounced compared to partly-coated soot particles during the transport through the sea pathway. Moreover, in contrast to the inland pathway, the D_f of embedded soot particles transported through the sea pathway showed a 9.5% greater amplitude (Figure 9). This comparative result is consistent with the observed differences in the D_p/D_c of soot-containing particles during two distinct atmospheric transport events (Figure 7), indicating that cloud process aging can greatly promote the structural collapse of soot aggregates. This mechanism can be ascribed to surface tension induced by the hygroscopic growth of secondary coatings on soot under elevated RH, which collapse the soot fractal morphology through water-mediated structural restructuring (Schnitzler et al., 2017). Therefore, cloud process aging of soot-containing particles during the transboundary transport through the sea pathway acted synergistically to (1) facilitate the entrainment of multiple soot cores, (2) substantially enhance their D_p/D_c ratios by ~50%, and (3) induce more pronounced collapse of soot fractal structures with D_f from 1.89 ± 0.06 to 2.07 ± 0.03.

3.4 Optical absorption of soot particles: inland vs. sea

Based on mixing structures of soot particles during the transboundary transport, the light absorption enhancement (E_{abs}) of soot-containing particles with 1-3 cores and different mixing structures (partly-coated and embedded configurations) was calculated

by the DDA combined with the EMBS. Considering that embedded soot cores were often distributed at the periphery rather than the center within individual particles (Figure 8), we conducted optical simulations of embedded soot-containing particles based on this realistic mixing structure. In the optical calculation, the diameters of single soot cores and coatings were presumed to 194 nm and 925 nm according to their size distribution (Figures S8 and 6d), and the total volume of soot cores in individual constructed particles was constant when their numbers were changed. Moreover, the coatings of soot cores were assumed to be non-absorbing materials in the optical calculation.

Figure 10a shows the change in the E_{abs} of soot-containing particles following their aging from bare-like to partly-coated, and then to embedded states. Compared to soot cores, partly-coated and embedded soot-containing particles present higher E_{abs} (Figure 10a), due to the lensing effect (Fierce et al., 2020; Wang et al., 2025). The E_{abs} of soot-containing particles with one soot core increased from 1.80 for the partly-coated structure to 2.83 for the embedded structure (Figure 10a). When soot-containing particles had two soot cores, the E_{abs} increased from 1.74 to 2.44, representing a 0.4-fold increase, with soot aging from partly-coated to embedded configurations (Figure 10a). Following the soot core number increase to three, the E_{abs} of soot-containing particles increased by 117% (from 1.04 to 2.26) when their mixing structures changed from partly-coated to embedded status (Figure 10a). These results suggest that individual particles containing higher numbers of soot cores demonstrate larger optical absorption amplification during atmospheric aging processes although their E_{abs} values were lower. Previous studies also found lower absorption efficiency in cloud drops with higher numbers of soot cores (Jacobson, 2006) and smaller E_{abs} in simulated ambient particles with larger number density of soot cores (Fierce et al., 2016). In addition, comparable radiative absorption changes for soot-containing particles with different numbers of soot cores were observed during the transformation of soot core positions (Zhang et al., 2022).

Based on the percentage, D_p/D_c, and E_{abs} of soot-containing particles with different

mixing structures and core numbers, we can compare the change in radiative absorption capacity per unit the change in coating thicknesses of soot-containing particles during the transboundary transport through the inland and the sea pathways. Figure 10b shows $\Delta E_{abs}/\Delta(D_p/D_c)$ of transboundary soot-containing particles transported through the inland and sea pathways. When soot-containing particles were transported from the NCP to the YRD through the inland pathway, their $\Delta E_{abs}/\Delta(D_p/D_c)$ reached 0.6 (Figure 10b). However, the $\Delta E_{abs}/\Delta(D_p/D_c)$ of soot-containing particles was only 0.17 following their transboundary transport through the sea pathway (Figure 10b). Previous studies have revealed that the E_{abs} of soot-containing particles first increases and then tends to stabilize with their coating thickness (e.g., D_p/D_c) increases (Beeler et al., 2024; Fu et al., 2022). We found that the mean D_p/D_c of embedded soot-containing particles exhibited a large value at 4.38 when haze masses were transported through the sea pathway (Figure 7b). In addition, cloud processes induced multiple soot cores within single particles during the transboundary transport through the sea pathway in contrast to the inland pathway, reducing their optical absorption (Figure 10a). Beeler et al. (2024) also found consistent results that much lower E_{abs} variation for soot-containing particles with the thickening of coatings in pyrocumulonimbus clouds compared with urban air. Therefore, the larger D_p/D_c change and the smaller E_{abs} change of soot-containing particles transported through the sea pathway should result in the lower $\Delta E_{abs}/\Delta(D_p/D_c)$ compared to those transported through the inland pathway. These findings further suggest that the radiative absorption amplification per unit D_p/D_c change of transboundary soot-containing particles reduced by 72% with the change in their transport pathways from inland to sea. A sensitivity test was conducted for the $\Delta E_{abs}/\Delta(D_p/D_c)$ reduction caused by the transport pathway change through varying the embedded soot core position in host particles, as shown in Figure S9. It was found that the $\Delta E_{abs}/\Delta(D_p/D_c)$ reduction is 68% when soot cores are randomly distributed in host particles (Figure S9). This is close to the 72% reduction calculated when soot cores are distributed at the periphery of host particles (Figure S9). Because over 80% of the embedded soot cores were observed to be distributed at the periphery of transboundary

particles, and the remainder was primarily randomly distributed, the 72% $\Delta E_{abs}/\Delta(D_p/D_c)$ reduction can be considered reliable. If embedded types in soot-containing particles were presumed as the traditional core-shell model, the $\Delta E_{abs}/\Delta(D_p/D_c)$ of transboundary soot-containing particles was extremely low at 0.01-0.03 (Table S3). This result shows a large difference from the optical absorption simulated with real mixing structures of soot-containing particles. Therefore, the traditional core-shell assumption significantly underestimates the optical absorption of transboundary soot-containing particles, which is consistent with findings in a wildfire smoke episode (Chen et al., 2025). It should be noted that the $\Delta E_{abs}/\Delta(D_p/D_c)$ derived from optical simulation is a conceptual metric, which depends on the chosen definition of D_p and D_c (e.g., ESD). While model–model comparisons are likely robust, model–measurement comparisons would likely require careful matching of definitions. In summary, the atmospheric humidity condition during the transport of soot particles not only affects their aging processes but also influences their radiative absorption (Figure 11). In view of that soot particles can be exposed to high-humidity or supersaturated atmospheric environments during transboundary transport, climate models should incorporate multicore soot-containing particles to refine current simulations of climate effects.

4. Conclusions and implications

Cold fronts triggered by the East Asian winter monsoon have frequently transported substantial air pollutant loads from the NCP to downwind areas over 1000 kilometers away in recent years, significantly impacting the YRD region (Huang et al., 2020; Zhao et al., 2021). To explore the variation in microphysical properties, mixing structures, and light absorption of soot particles in these haze pollutants and their aging mechanisms during the transboundary transport, we conducted synchronized field campaigns in December 2017 and December 2020 across the NCP and the YRD. Two types of transboundary transport models (i.e., passing through the inland and the sea) were identified based on transport pathways of haze plumes. According to the mixing

structure of soot particles examined by TEM observations, they were divided into bare-like, partly-coated, and embedded types. Meanwhile, the number of soot cores within individual soot-containing particles was quantified.

Following the transboundary transport of haze pollutants through the inland pathway, soot-containing particles underwent heterogeneous aging processes. This aging process changed the dominated mixing structure of soot-containing particles from partly-coated types at 67 ± 4% to embedded types at 71 ± 7%, but the soot core number per particle mainly remained at one. The median size and mean D_p/D_c of partly-coated and embedded soot-containing particles increased from 396-464 nm and 2.37-2.85 to 435-505 nm and 2.79-3.41 during the transboundary transport through the inland pathway because of secondary aerosol formation on soot particles via heterogeneous reactions. In addition, the soot core D_f increased from 1.81-1.90 to 1.84-1.93 under the compacting effect of secondary coatings on soot aggregates. When soot-containing particles were transported through the sea pathway, cloud process aging became their major evolution mechanisms. The cloud process aging not only transformed the dominated soot-containing particles from partly-coated types at 62 ± 1% to embedded types at 72 ± 4% but also increased their soot core numbers from 1 to ≥ 3. Compared to the inland pathway, the median size and mean D_p/D_c of partly-coated soot-containing particles and their soot core D_f showed similar variations during the transboundary transport through the sea pathway. However, these parameters for embedded soot-containing particles transported through the sea pathway represented larger increases from 446 nm, 2.92 ± 2.01, and 1.89 ± 0.06 in the NCP to 925 nm, 4.38 ± 2.92, and 2.07 ± 0.03 in the YRD.

Based on the optical simulation (assuming that coatings on soot are non-absorbing), transboundary soot-containing particles transported through the inland pathway exhibited a $\Delta E_{abs}/\Delta(D_p/D_c)$ of 0.6. Nevertheless, with the change in the transport pathway of soot-containing particles from the inland to the sea, the $\Delta E_{abs}/\Delta(D_p/D_c)$ reduced by 72% due to the entrainment of multiple soot cores by cloud processes. Our study demonstrates that soot particles undergo distinct evolutionary

processes and exhibit altered microphysical and optical properties across different transport pathways. This necessitates incorporating meteorological conditions along transport pathways, particularly the elevated RH in sea pathways, into future assessments of black carbon optical properties. Given the scarce observational data on transboundary black carbon in the marine atmosphere compared to well-characterized those in the inland atmosphere, directly applying inland-based parameterization schemes to simulate optical properties of black carbon transported through sea pathways would introduce significant biases. Therefore, to accurately obtain optical properties of atmospheric transported black carbon, we suggest that future studies should prioritize multiscale characterization of black carbon mixing structures and morphology in different transportation environments, particularly the cloud-processed mixing structure of multiple black carbon cores. Advanced single particle modeling, such as EMBS, that can reconstruct particles with real microphysical properties from TEM images could be coupled into macroscopic radiative forcing estimation (Wang et al., 2025). Ultimately, quantifying the climate impacts of black carbon necessitates a comprehensive understanding of how mixing structure and morphology evolution driven by atmospheric aging processes regulates absorption enhancement to refine predictive models for climate mitigation strategies.

Data availability

All data presented in this paper are available upon request from the corresponding author (liweijun@zju.edu.cn).

Author contributions

JZ and WL conceived the study and wrote the manuscript. The field campaigns were organized and supervised by JZ and WL, and assisted by YW, LX, YZ, and HN. JZ, YW, LX, and YZ contributed the sample analyses. ZZ made the optical simulation. All authors reviewed and commented on the paper.

Competing interests

The authors declare that they have no conflict of interest.

Acknowledgements

This work was funded by the National Natural Science Foundation of China (42307141 and 42307143), Shandong Provincial Natural Science Foundation of China (ZR2023QD094 and ZR2023QD151), Zhejiang Provincial Natural Science Foundation of China (LZJMZ25D050002), and LAC/CMA (2023B10). We thanked Wenshuai Li for the sea level pressure simulation.

References

Adachi, K., Zaizen, Y., Kajino, M., and Igarashi, Y.: Mixing state of regionally transported soot particles and the coating effect on their size and shape at a mountain site in Japan, J. Geophys. Res.-Atmos., 119, 5386-5396, https://doi.org/10.1002/2013jd020880, 2014.

Barone, T. L., Storey, J. M. E., Youngquist, A. D., and Szybist, J. P.: An analysis of direct-injection spark-ignition (DISI) soot morphology, Atmos. Environ., 49, 268-274, https://doi.org/10.1016/j.atmosenv.2011.11.047, 2012.

Beeler, P., Kumar, J., Schwarz, J. P., Adachi, K., Fierce, L., Perring, A. E., Katich, J. M., and Chakrabarty, R. K.: Light absorption enhancement of black carbon in a pyrocumulonimbus cloud, Nat. Commun., 15, 6243, https://doi.org/10.1038/s41467-024-50070-0, 2024.

Bond, T. C., and Bergstrom, R. W.: Light Absorption by Carbonaceous Particles: An Investigative Review, Aerosol Sci. Tech., 40, 27-67, https://doi.org/10.1080/02786820500421521, 2006.

Bond, T. C., Doherty, S. J., Fahey, D. W., Forster, P. M., Berntsen, T., DeAngelo, B. J., Flanner, M. G., Ghan, S., Kärcher, B., Koch, D., Kinne, S., Kondo, Y., Quinn, P. K., Sarofim, M. C., Schultz, M. G., Schulz, M., Venkataraman, C., Zhang, H., Zhang, S., Bellouin, N., Guttikunda, S. K., Hopke, P. K., Jacobson, M. Z., Kaiser, J. W., Klimont, Z., Lohmann, U., Schwarz, J. P., Shindell, D., Storelvmo, T., Warren, S. G., and Zender, C. S.: Bounding the role of black carbon in the climate system: A scientific assessment, J. Geophys. Res.-Atmos., 118, 5380-5552, https://doi.org/10.1002/jgrd.50171, 2013.

Cappa, C. D., Onasch, T. B., Massoli, P., Worsnop, D. R., Bates, T. S., Cross, E. S., Davidovits, P., Hakala, J., Hayden, K. L., Jobson, B. T., Kolesar, K. R., Lack, D. A., Lerner, B. M., Li, S. M., Mellon, D., Nuaaman, I., Olfert, J. S., Petaja, T., Quinn, P. K., Song, C., Subramanian, R., Williams, E. J., and Zaveri, R. A.: Radiative Absorption Enhancements Due to the Mixing State of Atmospheric Black Carbon, Science, 337, 1078-1081, https://doi.org/10.1126/science.1223447, 2012.

Chen, X., Ye, C., Wang, Y., Wu, Z., Zhu, T., Zhang, F., Ding, X., Shi, Z., Zheng, Z., and Li, W.: Quantifying evolution of soot mixing state from transboundary transport of biomass burning emissions, iScience, 26, 108125, https://doi.org/10.1016/j.isci.2023.108125, 2023.

Chen, X., Ching, J., Wu, F., Matsui, H., Jacobson, M. Z., Zhang, F., Wang, Y., Zhang, Z., Liu, D., Zhu, S., Rudich, Y., Shi, Z., Yoo, H., Jeon, K.-J., and Li, W.: Locating the missing absorption enhancement due to multi − core black carbon aerosols, Nat. Commun., 16, 10187, https://doi.org/10.1038/s41467-025-65079-2, 2025.

China, S., Scarnato, B., Owen, R. C., Zhang, B., Ampadu, M. T., Kumar, S., Dzepina, K., Dziobak, M. P., Fialho, P., Perlinger, J. A., Hueber, J., Helmig, D., Mazzoleni, L. R., and Mazzoleni, C.: Morphology and mixing state of aged soot particles at a remote marine free troposphere site: Implications for optical properties, Geophys. Res. Lett., 42, 1243-1250, https://doi.org/10.1002/2014gl062404, 2015.

Ding, S., Liu, D., Zhao, S., Wu, Y., Li, S., Pan, B., Teng, X., Li, W., Xu, W., Zhang, Y., Sun, Y., Wu, Y., Pan, X., Peng, X., Zhang, G., Bi, X., Tian, P., Liu, L., and Wang, Z.: Field Observation of Important Nonactivation Scavenging of Black Carbon by Clouds, Environ. Sci. Technol., 59, 9689-9698, https://doi.org/10.1021/acs.est.5c00199, 2025.

Farley, R. N., Collier, S., Cappa, C. D., Williams, L. R., Onasch, T. B., Russell, L. M., Kim, H., and Zhang, Q.: Source apportionment of soot particles and aqueous-phase processing of black carbon coatings in an urban environment, Atmos. Chem. Phys., 23, 15039-15056,

https://doi.org/10.5194/acp-23-15039-2023, 2023.
Fierce, L., Bond, T. C., Bauer, S. E., Mena, F., and Riemer, N.: Black carbon absorption at the global scale is affected by particle-scale diversity in composition, Nat. Commun., 7, 12361, https://doi.org/10.1038/ncomms12361, 2016.
Fierce, L., Onasch, T. B., Cappa, C. D., Mazzoleni, C., China, S., Bhandari, J., Davidovits, P., Fischer, D. A., Helgestad, T., Lambe, A. T., Sedlacek, A. J., Smith, G. D., and Wolff, L.: Radiative absorption enhancements by black carbon controlled by particle-to-particle heterogeneity in composition, Proc. Natl. Acad. Sci. U. S. A., 117, 5196-5203, https://doi.org/10.1073/pnas.1919723117, 2020.
Fu, Y., Peng, X., Sun, W., Hu, X., Wang, D., Yang, Y., Guo, Z., Wang, Y., Zhang, G., Zhu, J., Ou, J., Shi, Z., Wang, X., and Bi, X.: Impact of Cloud Process in the Mixing State and Microphysical Properties of Soot Particles: Implications in Light Absorption Enhancement, J. Geophys. Res.-Atmos., 127, e2022JD037169, https://doi.org/10.1029/2022JD037169, 2022.
Geng, G., Zheng, Y., Zhang, Q., Xue, T., Zhao, H., Tong, D., Zheng, B., Li, M., Liu, F., Hong, C., He, K., and Davis, S. J.: Drivers of PM2.5 air pollution deaths in China 2002–2017, Nat. Geosci., 14, 645-650, https://doi.org/10.1038/s41561-021-00792-3, 2021.
Han, C., Liu, Y., and He, H.: Role of Organic Carbon in Heterogeneous Reaction of NO2 with Soot, Environ. Sci. Technol., 47, 3174-3181, https://doi.org/10.1021/es304468n, 2013.
Hou, X., Zhu, B., Kumar, K. R., de Leeuw, G., Lu, W., Huang, Q., and Zhu, X.: Establishment of Conceptual Schemas of Surface Synoptic Meteorological Situations Affecting Fine Particulate Pollution Across Eastern China in the Winter, J. Geophys. Res.-Atmos., 125, e2020JD033153, https://doi.org/10.1029/2020JD033153, 2020.
Hu, X.-M., Hu, J., Gao, L., Cai, C., Jiang, Y., Xue, M., Zhao, T., and Crowell, S. M. R.: Multisensor and Multimodel Monitoring and Investigation of a Wintertime Air Pollution Event Ahead of a Cold Front Over Eastern China, J. Geophys. Res.-Atmos., 126, e2020JD033538, https://doi.org/10.1029/2020JD033538, 2021.
Huang, X., Ding, A., Wang, Z., Ding, K., Gao, J., Chai, F., and Fu, C.: Amplified transboundary transport of haze by aerosol–boundary layer interaction in China, Nat. Geosci., 13, 428–434, https://doi.org/10.1038/s41561-020-0583-4, 2020.
IPCC: Climate Change 2021: the Physical Science Basis: Contribution of Working Group I to the Sixth Assessment Report of the Intergovernmental Panel on Climate Change (IPCC). 2021.
Jacobson, M. Z.: Strong radiative heating due to the mixing state of black carbon in atmospheric aerosols, Nature, 409, 695-697, https://doi.org/10.1038/35055518, 2001.
Jacobson, M. Z.: Effects of Externally-Through-Internally-Mixed Soot Inclusions within Clouds and Precipitation on Global Climate, J. Phys. Chem. A, 110, 6860-6873, https://doi.org/10.1021/jp056391r, 2006.
Jin, X., Cai, X., Huang, Q., Wang, X., Song, Y., and Zhu, T.: Atmospheric Boundary Layer—Free Troposphere Air Exchange in the North China Plain and its Impact on PM2.5 Pollution, J. Geophys. Res.-Atmos., 126, e2021JD034641, https://doi.org/10.1029/2021JD034641, 2021.
Kang, H., Zhu, B., Gao, J., He, Y., Wang, H., Su, J., Pan, C., Zhu, T., and Yu, B.: Potential impacts of cold frontal passage on air quality over the Yangtze River Delta, China, Atmos. Chem. Phys., 19, 3673-3685, https://doi.org/10.5194/acp-19-3673-2019, 2019.
Lapuerta, M., Expósito, J. J., and Martos, F. J.: Effect of sintering on the fractal prefactor of agglomerates, Powder Technol., 271, 141-154, https://doi.org/10.1016/j.powtec.2014.10.041, 2015.

Li, B., Gasser, T., Ciais, P., Piao, S., Tao, S., Balkanski, Y., Hauglustaine, D., Boisier, J.-P., Chen, Z., Huang, M., Li, L. Z., Li, Y., Liu, H., Liu, J., Peng, S., Shen, Z., Sun, Z., Wang, R., Wang, T., Yin, G., Yin, Y., Zeng, H., Zeng, Z., and Zhou, F.: The contribution of China's emissions to global climate forcing, Nature, 531, 357-361, https://doi.org/10.1038/nature17165, 2016a.

Li, M., Wang, T., Xie, M., Li, S., Zhuang, B., Huang, X., Chen, P., Zhao, M., and Liu, J.: Formation and Evolution Mechanisms for Two Extreme Haze Episodes in the Yangtze River Delta Region of China During Winter 2016, J. Geophys. Res.-Atmos., 124, 3607-3623, https://doi.org/10.1029/2019JD030535, 2019.

Li, W., Sun, J., Xu, L., Shi, Z., Riemer, N., Sun, Y., Fu, P., Zhang, J., Lin, Y., Wang, X., Shao, L., Chen, J., Zhang, X., Wang, Z., and Wang, W.: A conceptual framework for mixing structures in individual aerosol particles, J. Geophys. Res.-Atmos., 121, 13784-13798, https://doi.org/10.1002/2016JD025252, 2016b.

Li, W., Riemer, N., Xu, L., Wang, Y., Adachi, K., Shi, Z., Zhang, D., Zheng, Z., and Laskin, A.: Microphysical properties of atmospheric soot and organic particles: measurements, modeling, and impacts, npj Clim. Atmos. Sci., 7, 65, https://doi.org/10.1038/s41612-024-00610-8, 2024.

Li, W., Ito, A., Wang, G., Zhi, M., Xu, L., Yuan, Q., Zhang, J., Liu, L., Wu, F., Laskin, A., Zhang, D., Zhang, X., Zhu, T., Chen, J., Mihalopoulos, N., Bougiatioti, A., Kanakidou, M., Wang, G., Hu, H., Zhao, Y., and Shi, Z.: Aqueous-phase secondary organic aerosol formation on mineral dust, Natl. Sci. Rev., 12, nwaf221, https://doi.org/10.1093/nsr/nwaf221, 2025.

Liu, D., He, C., Schwarz, J. P., and Wang, X.: Lifecycle of light-absorbing carbonaceous aerosols in the atmosphere, npj Clim. Atmos. Sci., 3, 40, https://doi.org/10.1038/s41612-020-00145-8, 2020.

Liu, L., Zhang, J., Xu, L., Yuan, Q., Huang, D., Chen, J., Shi, Z., Sun, Y., Fu, P., Wang, Z., Zhang, D., and Li, W.: Cloud scavenging of anthropogenic refractory particles at a mountain site in North China, Atmos. Chem. Phys., 18, 14681-14693, https://doi.org/10.5194/acp-18-14681-2018, 2018.

Niu, H., Hu, W., Zhang, D., Wu, Z., Guo, S., Pian, W., Cheng, W., and Hu, M.: Variations of fine particle physiochemical properties during a heavy haze episode in the winter of Beijing, Sci. Total Environ., 571, 103-109, https://doi.org/10.1016/j.scitotenv.2016.07.147, 2016.

Oh, C., and Sorensen, C. M.: The Effect of Overlap between Monomers on the Determination of Fractal Cluster Morphology, J. Colloid Interface Sci., 193, 17-25, https://doi.org/10.1006/jcis.1997.5046, 1997.

Pan, Y., Wang, Y., Sun, Y., Tian, S., and Cheng, M.: Size-resolved aerosol trace elements at a rural mountainous site in Northern China: importance of regional transport, Sci. Total Environ., 461-462, 761-771, https://doi.org/10.1016/j.scitotenv.2013.04.065, 2013.

Pang, Y., Wang, Y., Wang, Z., Zhang, Y., Liu, L., Kong, S., Liu, F., Shi, Z., and Li, W.: Quantifying the Fractal Dimension and Morphology of Individual Atmospheric Soot Aggregates, J. Geophys. Res.-Atmos., 127, e2021JD036055, https://doi.org/10.1029/2021JD036055, 2022.

Peng, J., Hu, M., Shang, D., Wu, Z., Du, Z., Tan, T., Wang, Y., Zhang, F., and Zhang, R.: Explosive Secondary Aerosol Formation during Severe Haze in the North China Plain, Environ. Sci. Technol., 55, 2189-2207, https://doi.org/10.1021/acs.est.0c07204, 2021.

Schnitzler, E. G., Gac, J. M., and Jäger, W.: Coating surface tension dependence of soot aggregate restructuring, J. Aerosol Sci., 106, 43-55, https://doi.org/10.1016/j.jaerosci.2017.01.005, 2017.

Sun, J., Liu, L., Xu, L., Wang, Y., Wu, Z., Hu, M., Shi, Z., Li, Y., Zhang, X., Chen, J., and Li, W.: Key Role of Nitrate in Phase Transitions of Urban Particles: Implications of Important Reactive Surfaces for Secondary Aerosol Formation, J. Geophys. Res.-Atmos., 123, 1234-1243,

https://doi.org/10.1002/2017JD027264, 2018.
Suzuki, K., and Takemura, T.: Perturbations to Global Energy Budget Due to Absorbing and Scattering Aerosols, J. Geophys. Res.-Atmos., 124, 2194-2209, https://doi.org/10.1029/2018jd029808, 2019.
Wang, J., Liu, D., Ge, X., Wu, Y., Shen, F., Chen, M., Zhao, J., Xie, C., Wang, Q., Xu, W., Zhang, J., Hu, J., Allan, J., Joshi, R., Fu, P., Coe, H., and Sun, Y.: Characterization of black carbon-containing fine particles in Beijing during wintertime, Atmos. Chem. Phys., 19, 447-458, https://doi.org/10.5194/acp-19-447-2019, 2019.
Wang, Q., Huang, R.-J., Zhao, Z., Cao, J., Ni, H., Tie, X., Zhao, S., Su, X., Han, Y., Shen, Z., Wang, Y., Zhang, N., Zhou, Y., and Corbin, J. C.: Physicochemical characteristics of black carbon aerosol and its radiative impact in a polluted urban area of China, J. Geophys. Res.-Atmos., 121, 12505-12519, https://doi.org/10.1002/2016JD024748, 2016.
Wang, Y., Liu, F., He, C., Bi, L., Cheng, T., Wang, Z., Zhang, H., Zhang, X., Shi, Z., and Li, W.: Fractal Dimensions and Mixing Structures of Soot Particles during Atmospheric Processing, Environ. Sci. Technol. Lett., 4, 487-493, https://doi.org/10.1021/acs.estlett.7b00418, 2017.
Wang, Y., Pang, Y., Huang, J., Bi, L., Che, H., Zhang, X., and Li, W.: Constructing Shapes and Mixing Structures of Black Carbon Particles With Applications to Optical Calculations, J. Geophys. Res.-Atmos., 126, e2021JD034620, https://doi.org/10.1029/2021JD034620, 2021.
Wang, Y., Zheng, Z., Sun, Y., Yao, Y., Ma, P.-L., Zhang, A., Zhu, S., Zhang, Z., Chen, X., Pang, Y., Wang, Q., Che, H., Ching, J., and Li, W.: Improved representation of black carbon mixing structures suggests stronger direct radiative heating, One Earth, 8, https://doi.org/10.1016/j.oneear.2025.101311, 2025.
Worringen, A., Ebert, M., Trautmann, T., Weinbruch, S., and Helas, G.: Optical properties of internally mixed ammonium sulfate and soot particles--a study of individual aerosol particles and ambient aerosol populations, Appl. Opt., 47, 3835-3845, https://doi.org/10.1364/AO.47.003835, 2008.
Wu, J., Bei, N., Li, X., Wang, R., Liu, S., Jiang, Q., Tie, X., and Li, G.: Impacts of Transboundary Transport on Coastal Air Quality of South China, J. Geophys. Res.-Atmos., 127, e2021JD036213, https://doi.org/10.1029/2021JD036213, 2022.
Wu, Y., Cheng, T., Zheng, L., and Chen, H.: Optical properties of the semi-external mixture composed of sulfate particle and different quantities of soot aggregates, J. Quant. Spectrosc. Radiat. Transfer, 179, 139-148, https://doi.org/10.1016/j.jqsrt.2016.03.012, 2016.
Wu, Y., Cheng, T., Liu, D., Allan, J. D., Zheng, L., and Chen, H.: Light Absorption Enhancement of Black Carbon Aerosol Constrained by Particle Morphology, Environ. Sci. Technol., 52, 6912-6919, https://doi.org/10.1021/acs.est.8b00636, 2018.
Xie, X., Hu, J., Qin, M., Guo, S., Hu, M., Ji, D., Wang, H., Lou, S., Huang, C., Liu, C., Zhang, H., Ying, Q., Liao, H., and Zhang, Y.: Evolution of atmospheric age of particles and its implications for the formation of a severe haze event in eastern China, Atmos. Chem. Phys., 23, 10563-10578, https://doi.org/10.5194/acp-23-10563-2023, 2023.
Xing, L., Fu, T. M., Cao, J. J., Lee, S. C., Wang, G. H., Ho, K. F., Cheng, M. C., You, C. F., and Wang, T. J.: Seasonal and spatial variability of the OM/OC mass ratios and high regional correlation between oxalic acid and zinc in Chinese urban organic aerosols, Atmos. Chem. Phys., 13, 4307-4318, https://doi.org/10.5194/acp-13-4307-2013, 2013.
Xu, L., Fukushima, S., Sobanska, S., Murata, K., Naganuma, A., Liu, L., Wang, Y., Niu, H., Shi, Z.,

Kojima, T., Zhang, D., and Li, W.: Tracing the evolution of morphology and mixing state of soot particles along with the movement of an Asian dust storm, Atmos. Chem. Phys., 20, 14321-14332, https://doi.org/10.5194/acp-20-14321-2020, 2020.

Yan, F., Su, H., Cheng, Y., Huang, R., Liao, H., Yang, T., Zhu, Y., Zhang, S., Sheng, L., Kou, W., Zeng, X., Xiang, S., Yao, X., Gao, H., and Gao, Y.: Frequent haze events associated with transport and stagnation over the corridor between the North China Plain and Yangtze River Delta, Atmos. Chem. Phys., 24, 2365-2376, https://doi.org/10.5194/acp-24-2365-2024, 2024.

Yuan, Q., Xu, J., Wang, Y., Zhang, X., Pang, Y., Liu, L., Bi, L., Kang, S., and Li, W.: Mixing State and Fractal Dimension of Soot Particles at a Remote Site in the Southeastern Tibetan Plateau, Environ. Sci. Technol., 53, 8227-8234, https://doi.org/10.1021/acs.est.9b01917, 2019.

Zang, H., Zhao, Y., Huo, J., Zhao, Q., Fu, Q., Duan, Y., Shao, J., Huang, C., An, J., Xue, L., Li, Z., Li, C., and Xiao, H.: High atmospheric oxidation capacity drives wintertime nitrate pollution in the eastern Yangtze River Delta of China, Atmos. Chem. Phys., 22, 4355-4374, https://doi.org/10.5194/acp-22-4355-2022, 2022.

Zhai, S., Jacob, D. J., Wang, X., Liu, Z., Wen, T., Shah, V., Li, K., Moch, J. M., Bates, K. H., Song, S., Shen, L., Zhang, Y., Luo, G., Yu, F., Sun, Y., Wang, L., Qi, M., Tao, J., Gui, K., Xu, H., Zhang, Q., Zhao, T., Wang, Y., Lee, H. C., Choi, H., and Liao, H.: Control of particulate nitrate air pollution in China, Nat. Geosci., 14, 389-395, https://doi.org/10.1038/s41561-021-00726-z, 2021.

Zhang, J., Liu, L., Wang, Y., Ren, Y., Wang, X., Shi, Z., Zhang, D., Che, H., Zhao, H., Liu, Y., Niu, H., Chen, J., Zhang, X., Lingaswamy, A. P., Wang, Z., and Li, W.: Chemical composition, source, and process of urban aerosols during winter haze formation in Northeast China, Environ. Pollut., 231, 357-366, https://doi.org/10.1016/j.envpol.2017.07.102, 2017a.

Zhang, J., Yuan, Q., Liu, L., Wang, Y., Zhang, Y., Xu, L., Pang, Y., Zhu, Y., Niu, H., Shao, L., Yang, S., Liu, H., Pan, X., Shi, Z., Hu, M., Fu, P., and Li, W.: Trans-Regional Transport of Haze Particles From the North China Plain to Yangtze River Delta During Winter, J. Geophys. Res.-Atmos., 126, e2020JD033778, https://doi.org/10.1029/2020JD033778, 2021.

Zhang, J., Wang, Y., Teng, X., Liu, L., Xu, Y., Ren, L., Shi, Z., Zhang, Y., Jiang, J., Liu, D., Hu, M., Shao, L., Chen, J., Martin, S. T., Zhang, X., and Li, W.: Liquid-liquid phase separation reduces radiative absorption by aged black carbon aerosols, Commun. Earth Environ., 3, 128, https://doi.org/10.1038/s43247-022-00462-1, 2022.

Zhang, J., Li, W., Wang, Y., Teng, X., Zhang, Y., Xu, L., Yuan, Q., Wu, G., Niu, H., and Shao, L.: Structural Collapse and Coating Composition Changes of Soot Particles During Long-Range Transport, J. Geophys. Res.-Atmos., 128, e2023JD038871, https://doi.org/10.1029/2023JD038871, 2023.

Zhang, Q., Jiang, X., Tong, D., Davis, S. J., Zhao, H., Geng, G., Feng, T., Zheng, B., Lu, Z., and Streets, D. G.: Transboundary health impacts of transported global air pollution and international trade, Nature, 543, 705-709, https://doi.org/10.1038/nature21712, 2017b.

Zhang, W., Zhang, Y.-L., Cao, F., Xiang, Y., Zhang, Y., Bao, M., Liu, X., Lin, Y.-C. J. A. C., and Physics: High time-resolved measurement of stable carbon isotope composition in water-soluble organic aerosols: method optimization and a case study during winter haze in eastern China, Atmos. Chem. Phys., 19, 11071-11087, https://doi.org/10.5194/acp-19-11071-2019, 2019a.

Zhang, Y., Zhang, Q., Cheng, Y., Su, H., Li, H., Li, M., Zhang, X., Ding, A., and He, K.: Amplification of light absorption of black carbon associated with air pollution, Atmos. Chem. Phys., 18, 9879-9896, https://doi.org/10.5194/acp-18-9879-2018, 2018.

Zhang, Y., Li, M., Cheng, Y., Geng, G., Hong, C., Li, H., Li, X., Tong, D., Wu, N., Zhang, X., Zheng, B., Zheng, Y., Bo, Y., Su, H., and Zhang, Q.: Modeling the aging process of black carbon during atmospheric transport using a new approach: a case study in Beijing, Atmos. Chem. Phys., 19, 9663-9680, https://doi.org/10.5194/acp-19-9663-2019, 2019b.

Zhao, J., Qiu, Y., Zhou, W., Xu, W., Wang, J., Zhang, Y., Li, L., Xie, C., Wang, Q., Du, W., Worsnop, D. R., Canagaratna, M. R., Zhou, L., Ge, X., Fu, P., Li, J., Wang, Z., Donahue, N. M., and Sun, Y.: Organic Aerosol Processing During Winter Severe Haze Episodes in Beijing, J. Geophys. Res.-Atmos., 124, 10248-10263, https://doi.org/10.1029/2019jd030832, 2019.

Zhao, S., Feng, T., Tie, X., Li, G., and Cao, J.: Air Pollution Zone Migrates South Driven by East Asian Winter Monsoon and Climate Change, Geophys. Res. Lett., 48, e2021GL092672, https://doi.org/10.1029/2021GL092672, 2021.

Zheng, G. J., Duan, F. K., Su, H., Ma, Y. L., Cheng, Y., Zheng, B., Zhang, Q., Huang, T., Kimoto, T., Chang, D., Pöschl, U., Cheng, Y. F., and He, K. B.: Exploring the severe winter haze in Beijing: the impact of synoptic weather, regional transport and heterogeneous reactions, Atmos. Chem. Phys., 15, 2969-2983, https://doi.org/10.5194/acp-15-2969-2015, 2015.

Zhong, J., Zhang, X., Wang, Y., Wang, J., Shen, X., Zhang, H., Wang, T., Xie, Z., Liu, C., Zhang, H., Zhao, T., Sun, J., Fan, S., Gao, Z., Li, Y., and Wang, L.: The two-way feedback mechanism between unfavorable meteorological conditions and cumulative aerosol pollution in various haze regions of China, Atmos. Chem. Phys., 19, 3287-3306, https://doi.org/10.5194/acp-19-3287-2019, 2019.

Zhu, J., Wu, S., Yue, H., Gao, E., Wang, W., Li, J., Wu, Z., and Yao, S.: Enhanced oxidative potential and SO2 heterogeneous oxidation on candle soot after photochemical aging: Influencing mechanisms of different irradiation wavelengths, Environ. Pollut., 367, 125583, https://doi.org/10.1016/j.envpol.2024.125583, 2025.

Figure Captions

Figure 1. Meteorological fields in eastern China during the observation period. (a-b) Wind fields combined with surface $PM_{2.5}$ concentrations at 20:00 (local time) on December 30, 2017 and at 2:00 on December 8, 2020 derived from European Centre for Medium-Range Weather Forecasts (ECMWF, https://earth.nullschool.net/). The blue arrow dashed lines indicate prevailing wind direction. (c-d) Meteorological fields covering observation sites in the North China Plain (NCP) and Yangtze River Delta (YRD) at 1000 hpa.

Figure 2. Concentration-weighted trajectory (CWT) plots of $PM_{2.5}$ before arriving at observation sites (Nanjing and Hangzhou) in the YRD. (a-b) Transboundary transport through the inland pathway during December 30-31, 2017. (c-d) Transboundary transport through the sea pathway during December 7-8, 2020.

Figure 3. Typical transmission electron microscopy (TEM) images of soot particles in different mixing structures. (a) Bare-like soot particle. (b) Partly-coated soot particles. (c) Embedded soot particles. Some indiscernible embedded soot particles in panel (c) can be clearly observed after their coatings are sublimed under an enhanced electron beam.

Figure 4. Typical TEM images and number fractions of soot-containing particles with different mixing structures and soot core numbers in two types of transboundary transport models from the NCP to the YRD. (a) Partly-coated and embedded soot-containing particles with different numbers of soot cores. (b) Variation in the number fraction of soot-containing particles during the transboundary transport through the inland pathway. (c) Variation in the number fraction of soot-containing particles during the transboundary transport through the sea pathway.

Figure 5. Number fractions of soot-containing particles with different mixing structures and numbers of soot cores in different size bins in two types of transboundary transport models from the NCP to the YRD. (a-b) Soot-containing particles transported through the inland pathway. (c-d) Soot-containing particles transported through the sea pathway.

Figure 6. Number size distribution of soot-containing particles in two types of

transboundary transport models from the NCP to the YRD. (a-b) Size distribution of soot-containing particles transported through the inland pathway. (c-d) Size distribution of soot-containing particles transported through the sea pathway.

Figure 7. The size ratio of soot-containing particles to their soot cores (D_p/D_c) in two types of transboundary transport models from the NCP to the YRD. (a) D_p/D_c ratios of soot-containing particles transported through the inland pathway. (b) D_p/D_c ratios of soot-containing particles transported through the sea pathway. A schematic model of the D_p/D_c ratio of soot-containing particles with the core-shell structure is exampled.

Figure 8. Low magnification TEM images of soot-containing particles in the YRD during two transboundary transport. (a) Soot-containing particles transported through the inland pathway. (b) Soot-containing particles transported through the sea pathway. (c-d) Magnified TEM images for soot-containing particles in panel (a). (e-f) Magnified TEM images for soot-containing particles in panel (b).

Figure 9. Variation in the fractal dimension (D_f) of partly-coated and embedded soot particles during their transboundary transport from the NCP to the YRD. (a-b) D_f of soot particles transported through the inland pathway. (c-d) D_f of soot particles transported through the sea pathway. A schematic model of the soot D_f is exemplified.

Figure 10. Variation in the optical absorption of soot-containing particles. (a) The light absorption enhancement (E_{abs}) of partly-coated and embedded soot-containing particle models relative to their soot cores. (b) The change in E_{abs} per unit the change in D_p/D_c ($\Delta E_{abs}/\Delta(D_p/D_c)$) of soot-containing particles during two transboundary transport events through the inland and the sea pathways. Partly-coated and embedded soot-containing particle models constructed by the Electron-Microscope-to-BC-Simulation (EMBS) tool were exampled in panel (a).

Figure 11. A schematic diagram for the change in the mixing structure and optical absorption of soot-containing particles during the transboundary transport from the NCP to the YRD through the inland and the sea pathways. (a) Soot-containing particles undergo heterogeneous aging processes during the transboundary transport through the inland pathway, which mainly change their mixing structures from partly-coated with

single soot core to embedded with single soot core structures and increase the E_{abs} change per unit D_p/D_c change at 0.6. (b) Following the transboundary transport of soot-containing particles through the sea pathway, cloud process aging becomes the dominated evolution mechanism of soot-containing particles. This process not only transforms the mixing structure of soot-containing particles from partly-coated with single soot core to embedded with multiple soot core structures but also slightly enhances the E_{abs} change per unit D_p/D_c change at 0.17.

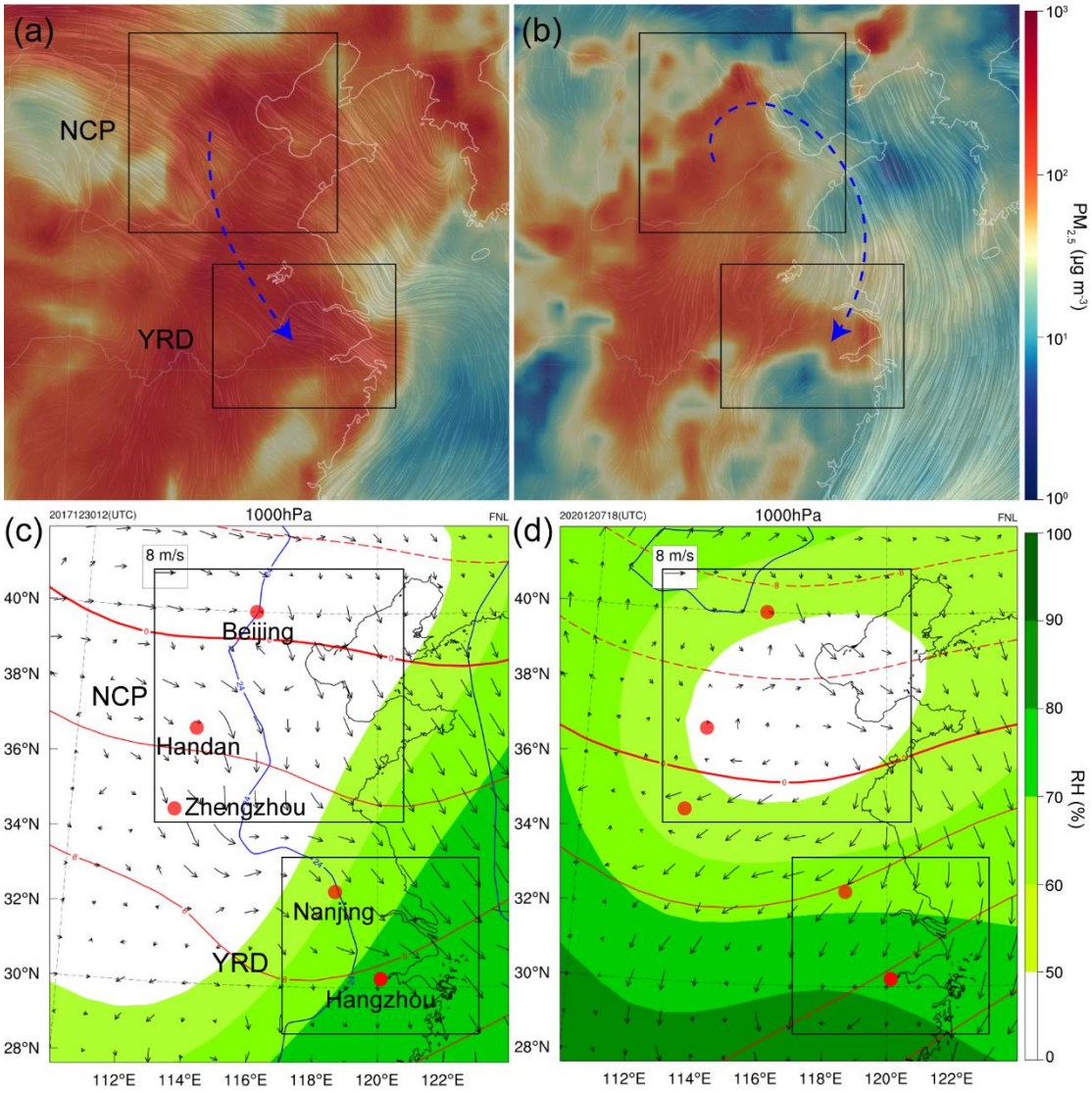

Figure 1. Meteorological fields in eastern China during the observation period. (a-b) Wind fields combined with surface $PM_{2.5}$ concentrations at 20:00 (local time) on December 30, 2017 and at 2:00 on December 8, 2020 derived from European Centre for Medium-Range Weather Forecasts (ECMWF, https://earth.nullschool.net/). The blue arrow dashed lines indicate prevailing wind direction. (c-d) Meteorological fields covering observation sites in the North China Plain (NCP) and Yangtze River Delta (YRD) at 1000 hpa.

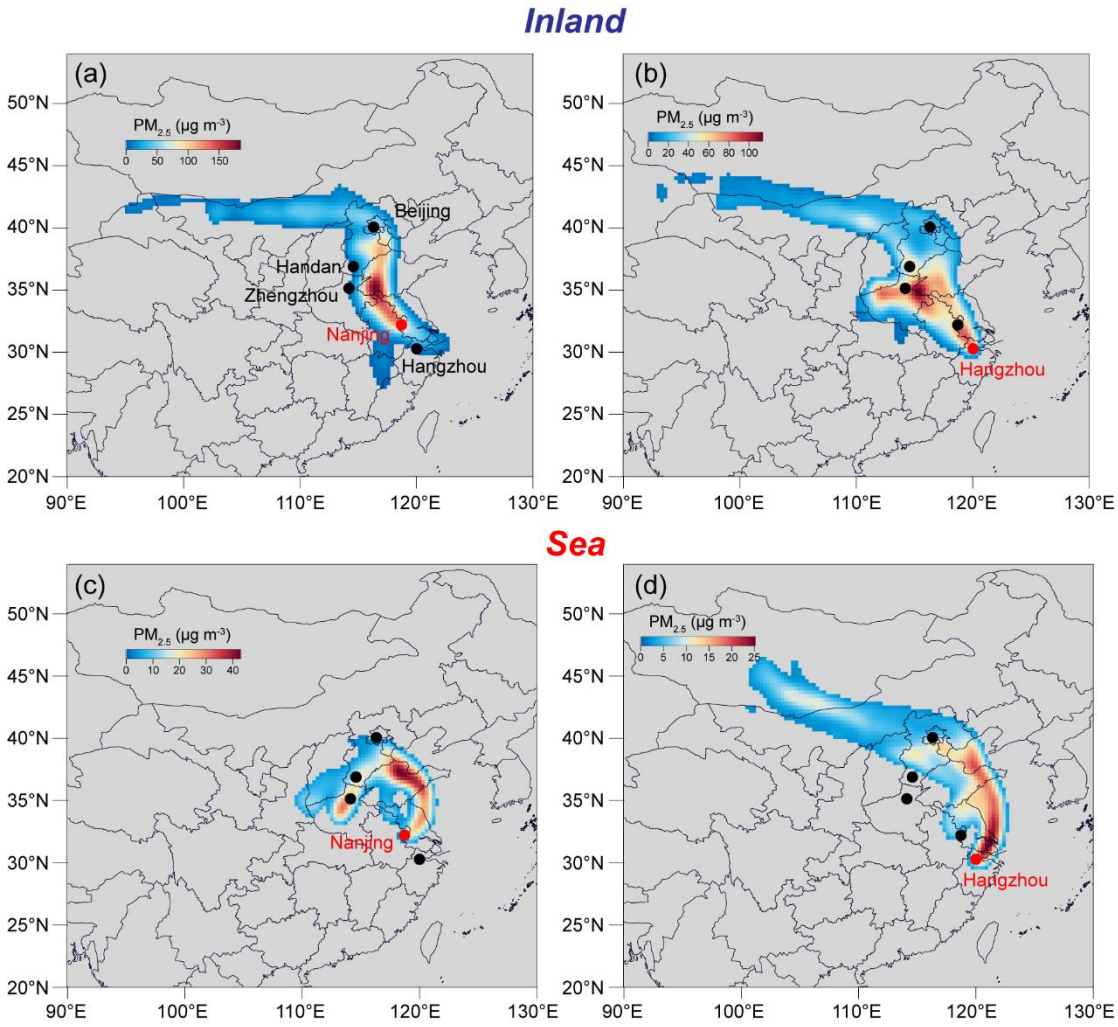

Figure 2. Concentration-weighted trajectory (CWT) plots of $PM_{2.5}$ before arriving at observation sites (Nanjing and Hangzhou) in the YRD. (a-b) Transboundary transport through the inland pathway during December 30-31, 2017. (c-d) Transboundary transport through the sea pathway during December 7-8, 2020.

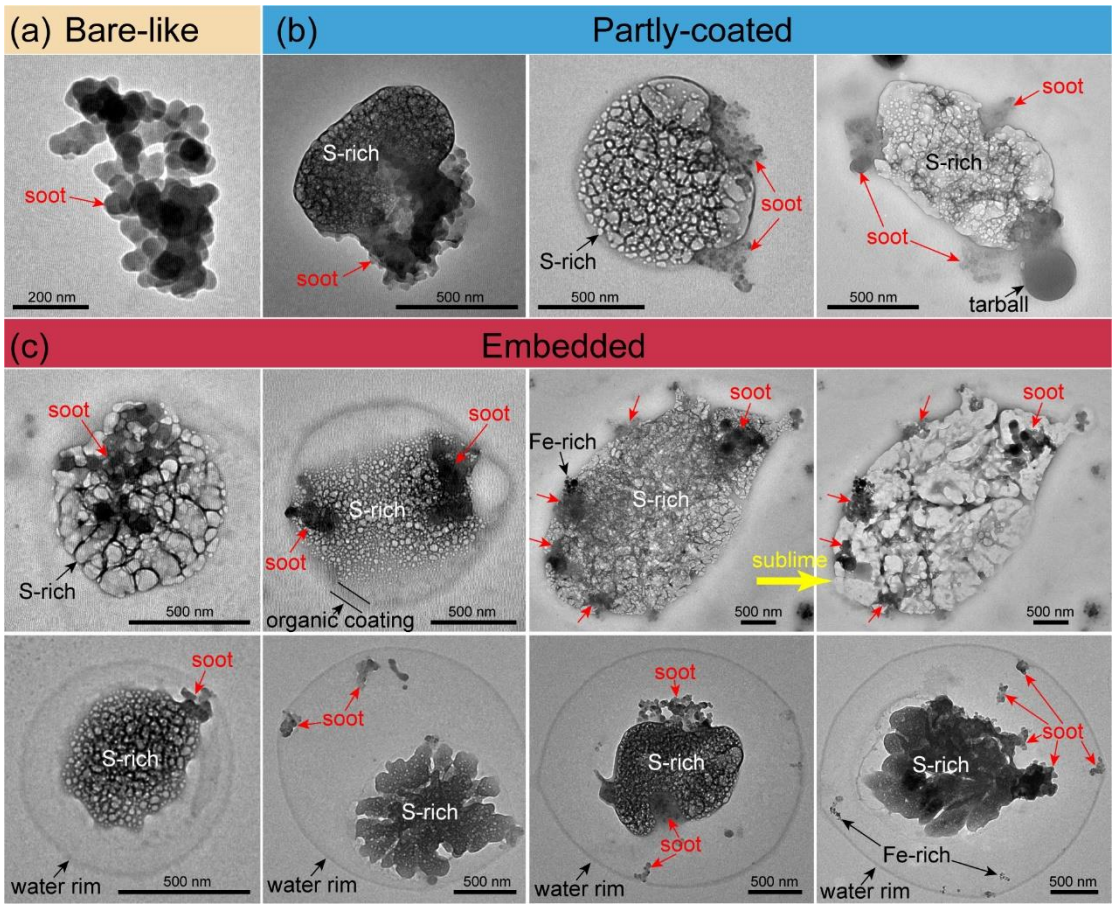

Figure 3. Typical transmission electron microscopy (TEM) images of soot particles in different mixing structures. (a) Bare-like soot particle. (b) Partly-coated soot particles. (c) Embedded soot particles. Some indiscernible embedded soot particles in panel (c) can be clearly observed after their coatings are sublimed under an enhanced electron beam.

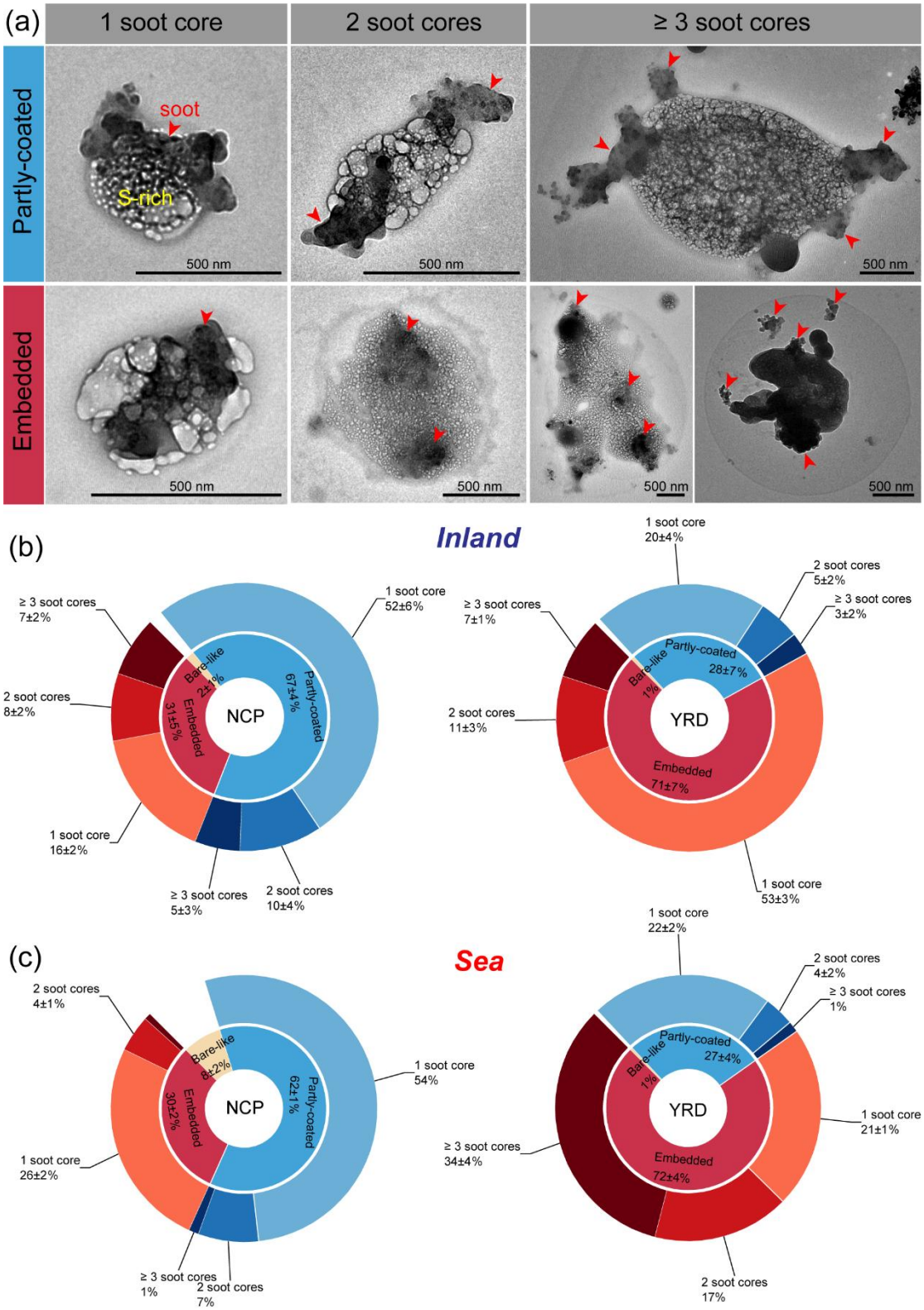

Figure 4. Typical TEM images and number fractions of soot-containing particles with different mixing structures and soot core numbers in two types of transboundary transport models from the NCP to the YRD. (a) Partly-coated and embedded soot-containing particles with different numbers of soot cores. (b) Variation in the number

1009 fraction of soot-containing particles during the transboundary transport through the
1010 inland pathway. (c) Variation in the number fraction of soot-containing particles during
1011 the transboundary transport through the sea pathway.

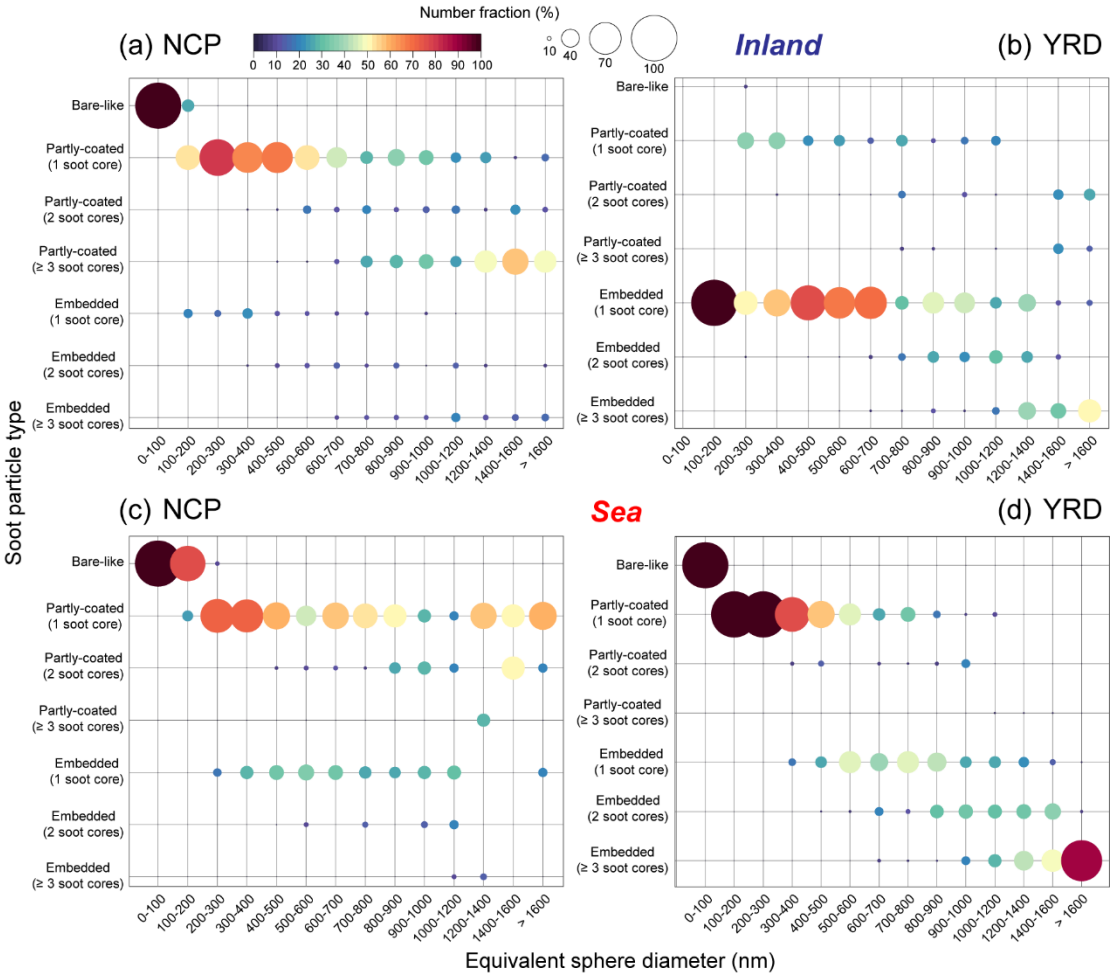

Figure 5. Number fractions of soot-containing particles with different mixing structures and numbers of soot cores in different size bins in two types of transboundary transport models from the NCP to the YRD. (a-b) Soot-containing particles transported through the inland pathway. (c-d) Soot-containing particles transported through the sea pathway.

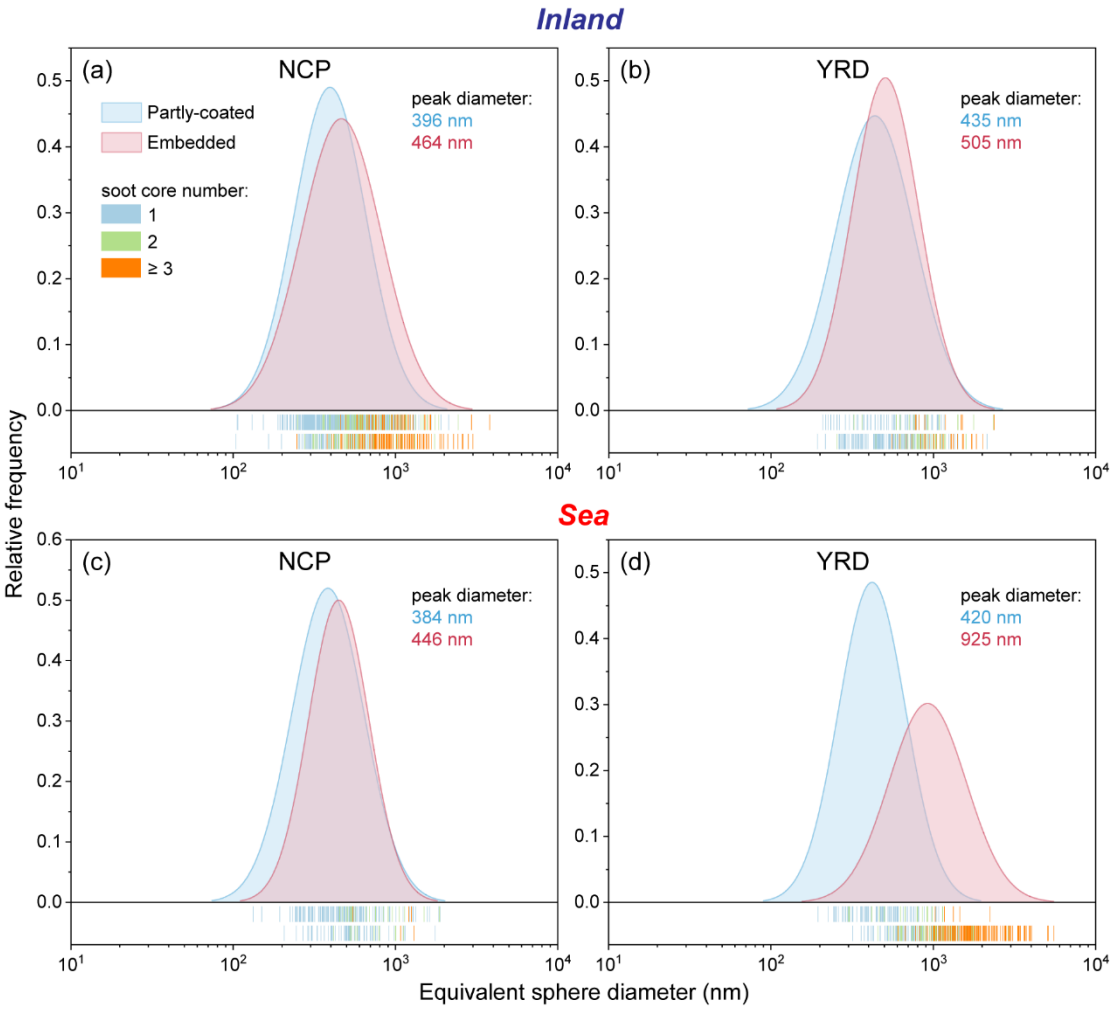

1017

1018 **Figure 6.** Number size distribution of soot-containing particles in two types of
1019 transboundary transport models from the NCP to the YRD. (a-b) Size distribution of
1020 soot-containing particles transported through the inland pathway. (c-d) Size distribution
1021 of soot-containing particles transported through the sea pathway.

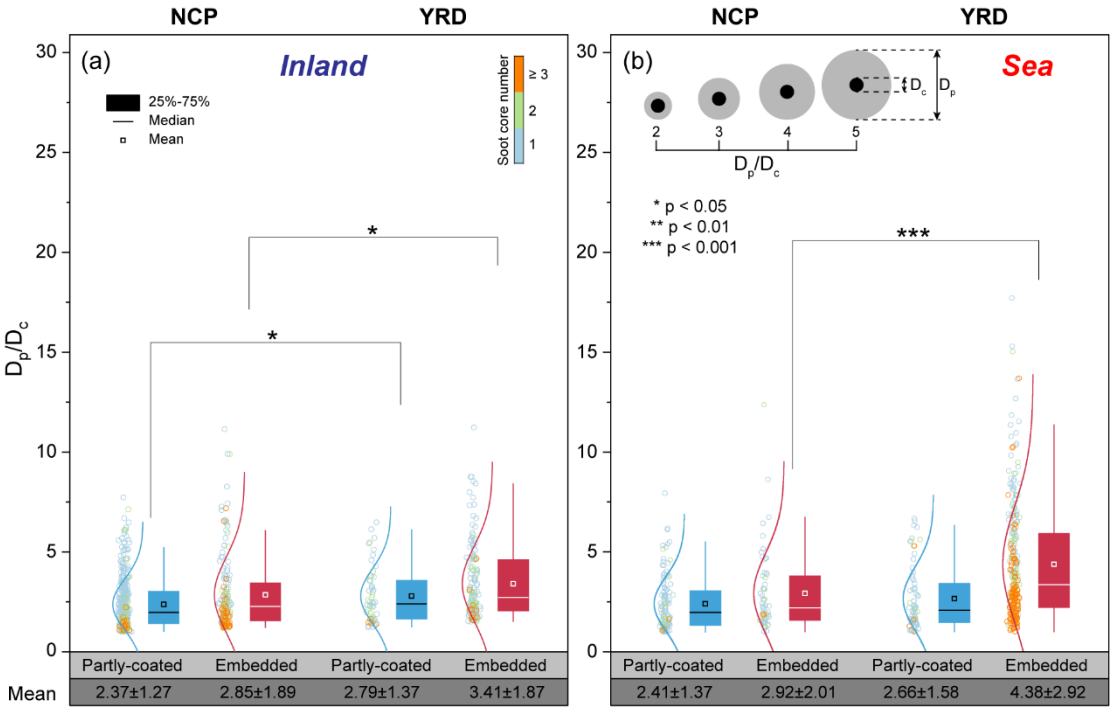

Figure 7. The size ratio of soot-containing particles to their soot cores (D_p/D_c) in two types of transboundary transport models from the NCP to the YRD. (a) D_p/D_c ratios of soot-containing particles transported through the inland pathway. (b) D_p/D_c ratios of soot-containing particles transported through the sea pathway. A schematic model of the D_p/D_c ratio of soot-containing particles with the core-shell structure is exampled.

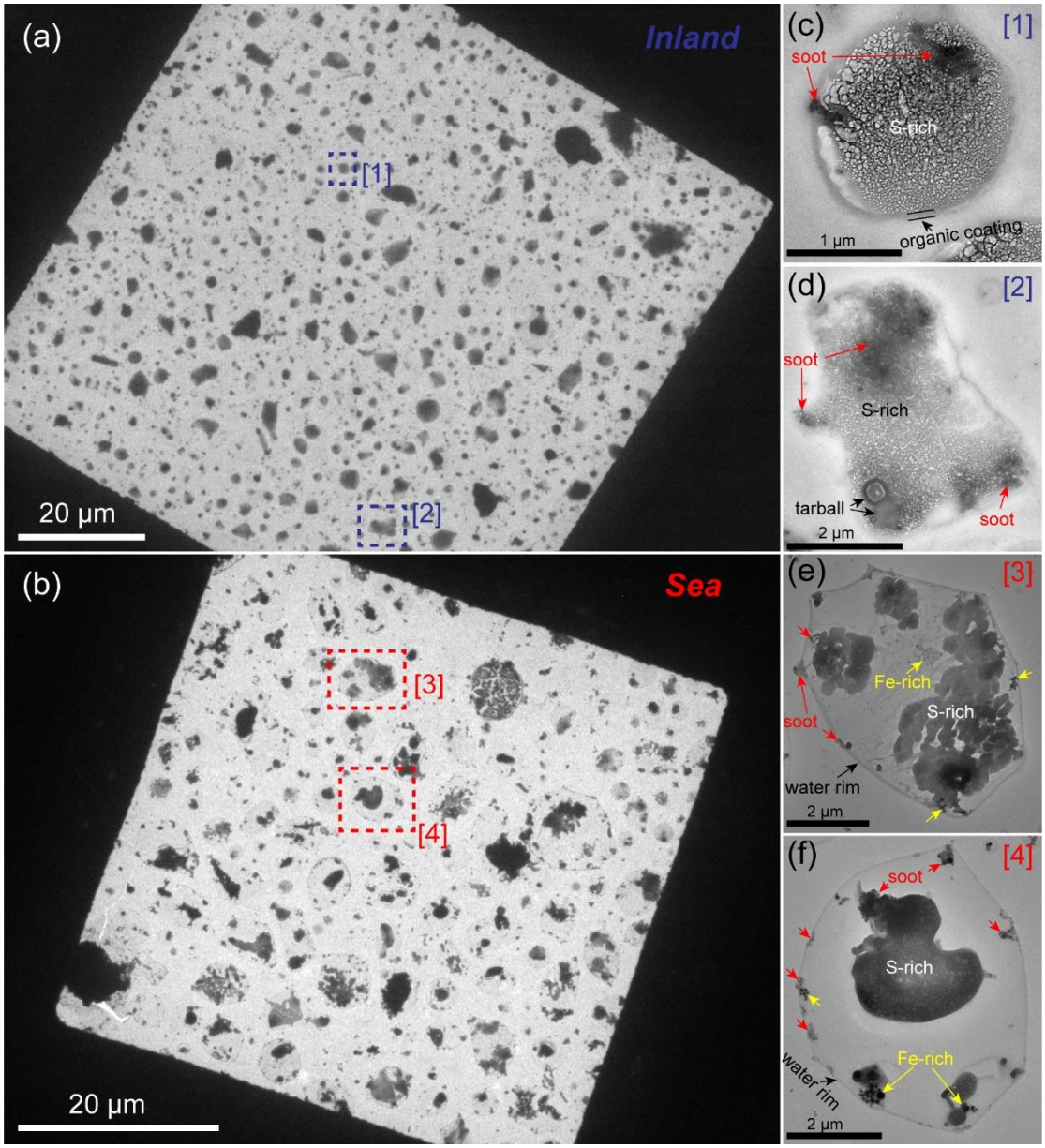

Figure 8. Low magnification TEM images of soot-containing particles in the YRD during two transboundary transport. (a) Soot-containing particles transported through the inland pathway. (b) Soot-containing particles transported through the sea pathway. (c-d) Magnified TEM images for soot-containing particles in panel (a). (e-f) Magnified TEM images for soot-containing particles in panel (b).

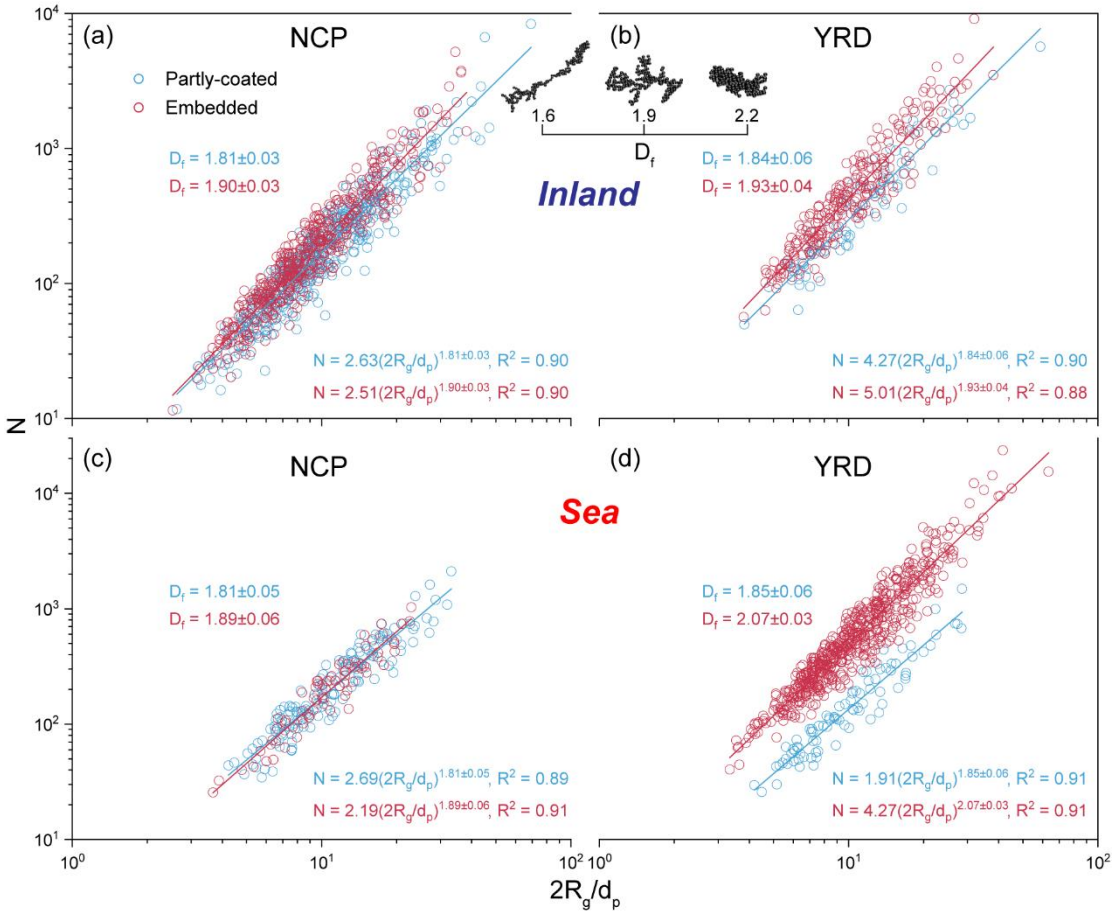

Figure 9. Variation in the fractal dimension (D_f) of partly-coated and embedded soot particles during their transboundary transport from the NCP to the YRD. (a-b) D_f of soot particles transported through the inland pathway. (c-d) D_f of soot particles transported through the sea pathway. A schematic model of the soot D_f is exemplified.

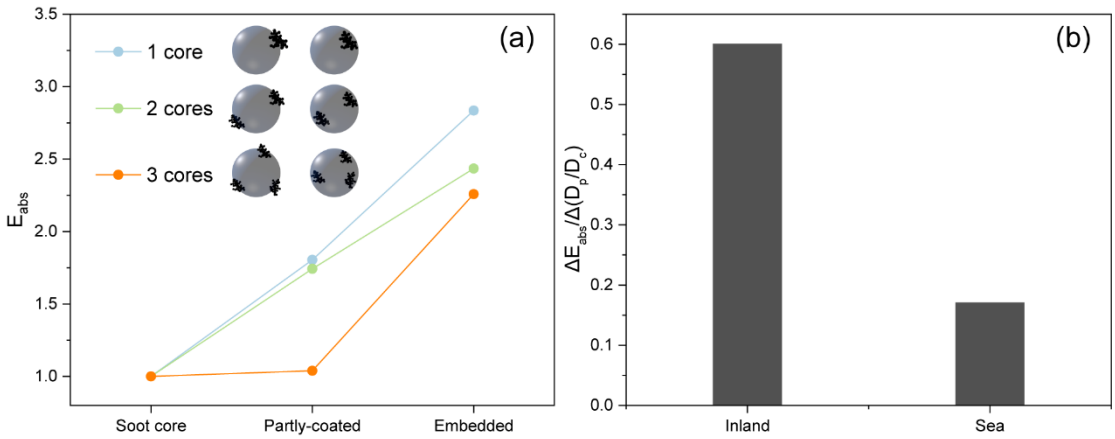

Figure 10. Variation in the optical absorption of soot-containing particles. (a) The light absorption enhancement (E_{abs}) of partly-coated and embedded soot-containing particle models relative to their soot cores. (b) The change in E_{abs} per unit the change in D_p/D_c ($\Delta E_{abs}/\Delta(D_p/D_c)$) of soot-containing particles during two transboundary transport events through the inland and the sea pathways. Partly-coated and embedded soot-containing particle models constructed by the Electron-Microscope-to-BC-Simulation (EMBS) tool were exampled in panel (a).

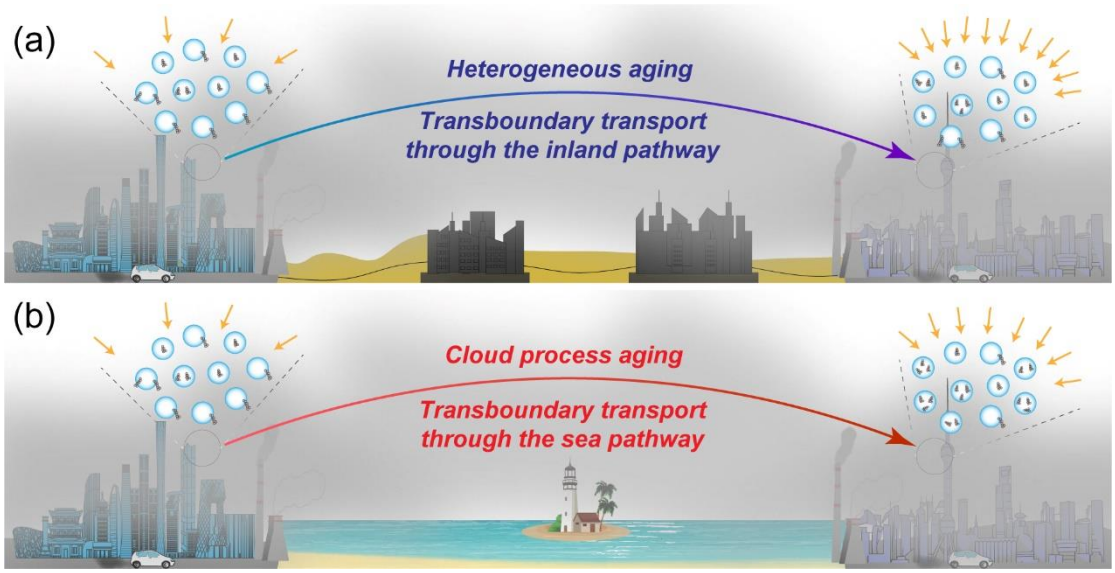

Figure 11. A schematic diagram for the change in the mixing structure and optical absorption of soot-containing particles during the transboundary transport from the NCP to the YRD through the inland and the sea pathways. (a) Soot-containing particles undergo heterogeneous aging processes during the transboundary transport through the inland pathway, which mainly change their mixing structures from partly-coated with single soot core to embedded with single soot core structures and increase the E_{abs} change per unit D_p/D_c change at 0.6. (b) Following the transboundary transport of soot-containing particles through the sea pathway, cloud process aging becomes the dominated evolution mechanism of soot-containing particles. This process not only transforms the mixing structure of soot-containing particles from partly-coated with single soot core to embedded with multiple soot core structures but also slightly enhances the E_{abs} change per unit D_p/D_c change at 0.17.